Understanding the Corrosion of Low-Voltage Al-Ga Anodes

Devon Scott Baker

Thesis submitted to the faculty of
Virginia Polytechnic Institute and State University
In partial fulfillment of the requirements for the degree of

Master of Science
in
Materials Science and Engineering

Alan P. Druschitz, Chair
William T. Reynolds
Sean G. Corcoran

May 4th, 2015
Blacksburg, VA

Keywords: aluminum, gallium, anodes, seawater, corrosion

Understanding the Corrosion of Low-Voltage Al-Ga Anodes

Devon Scott Baker

ABSTRACT

Aluminum is an attractive metal for use as an anode in the cathodic protection of steels in seawater due to its low cost and high current capacity. Zinc is often used for its ability to readily corrode, but it has a low current capacity and it operates at very negative voltages, leading to hydrogen generation at the steel cathode, which may cause hydrogen embrittlement. Aluminum can operate at less-negative voltages, therefore reducing hydrogen generation, but it forms a passive oxide film, preventing the anode from corroding. Ga is added to aluminum in small amounts (0.1 wt%) to destabilize this oxide film and allow for active corrosion. The mechanism of how Ga activates Al is still not well-known, though there are prevailing proposals. A previous study noted a difference in behavior between Al-Ga master heats and the alloys that were later produced by re-melting them. This study is focused on characterizing the corrosion behavior of Al-0.1 wt% Ga in synthetic seawater, with samples from a master heat and two subsequent remelts. Galvanostatic, potentiostatic, and open-circuit tests were run, as well as galvanic coupling with 1123 steel. It was found that the remelted anodes behaved more consistently and maintained stable corrosion behavior for longer times than the master heat. X-ray Photoelectron Spectroscopy analysis showed elevated concentrations of Ga inside the oxide layer. The findings support the mechanism in the literature of discrete particles of Ga forming under the oxide film but do not support the mechanism of an amalgam layer formation. This project was funded by NACE International, Virginia Tech project number 457789.

Acknowledgements

I would like to thank my advisor, Dr. Alan Druschitz, for the wisdom, guidance, and support he has given me over the past three years. It was through his teaching that I discovered my passion for cast metals and metallurgy, so I have him to thank for showing me what I want to do for the rest of my life.

I would like to thank my other committee members, Dr. William Reynolds and Dr. Sean Corcoran, for their instruction and advice through this project as well as throughout my undergraduate and graduate studies at Virginia Tech.

I would like to thank NACE International for supplying the funding for this project, Virginia Tech project number 457789, via a research seed grant; without that funding this project would not have been possible.

I would like to thank Steve McCartney and Andrew Giordani at NCFL for their assistance with the SEM and XPS.

I would like to thank Jacob Monzel for his prior work on this subject; it gave me a solid foundation to work from.

I would like to thank the MSE department for allowing me this opportunity to further my education.

I would like to thank my family for their continued love and support. Mom, Papa, Rob, Kelcey, Rowan, Bjorn, thank you for showing me you love me.

I would like to thank my friends for their love and support during the best and worst of times, especially El, Camilla, Em, Ross, Ken, and Andy.

I would most of all like to thank Rhit, for showing me love and understanding beyond what I thought possible, for supporting me unwaveringly through these past eight months, and for staying up late with me while I write this.

Table of Contents

List of Figures

List of Tables

1. Introduction

1.1 Author's Note

For the sake of clarity and consistency, all potentials given in this thesis are in reference to a saturated calomel electrode (SCE). The title of this work refers to anodes operating at small-magnitude negative potentials, but the terms "higher potential" and "lower potential" (as well as other qualitative comparisons such as "maximum/minimum") will refer to less negative and more negative potentials, respectively, e.g. a potential of -1500 mV will be lower than a potential of -1000 mV.

1.2 Background on Galvanic Corrosion and Sacrificial Anodes

The study of galvanic corrosion dates back to 1824, when Sir Humphry Davy was commissioned by the British Navy to determine why the copper sheeting on their ships was corroding. He first found that the corrosion of the copper was not due to impurities in the alloy, and that in fact pure copper corroded faster than the alloys [1]. He then supposed that the corrosion must be caused by oxygen dissolved in the seawater [1]. Building off earlier work where he found that reactions may be controlled by "the electrical states of bodies", he figured that "if [copper] could be rendered slightly negative, the corroding action of sea water upon it would be null" [1]. To make the copper "slightly negative" would involve attaching metals to it that were used with copper in a voltaic battery, such as tin, zinc, and iron [1]. Tin was very effective at protecting the copper, but it eventually formed a passive chloride, allowing the copper to resume corrosion [1]. Zinc and iron were both effective protectors and did not passivate over time [1]. The zinc was also found to protect the iron when all three were electrically connected [1]. Ultimately, however, this solution was not put into practice for long, because it turned out that copper ions in seawater have excellent anti-fouling properties, so when the copper was protected from corrosion, the boat hulls acquired tremendous buildups of marine life such as algae and barnacles [2].

It is now known that each metal has a particular equilibrium potential in a given electrolyte, and that when two dissimilar metals are put into electrical contact in that electrolyte, the difference in their potentials drives the corrosion of the more active metal, the one with the lower potential [3]. This is known as galvanic corrosion. When metals are ranked in order from most to least noble, particularly in seawater, this ranking is called the galvanic series [3].

Preventing the corrosion of iron and steel in water, particularly seawater, is extremely important. The way to accomplish this is to force the iron or steel to become a cathode, and there are two methods for doing so: active protection, which involves impressing a current upon the iron or steel in order to bring its potential within a cathodic range; or the more common method of passive protection (often called cathodic protection), which involves attaching a more active metal to the iron or steel, protecting it via galvanic corrosion [2, 3]. This more active metal is called a sacrificial anode, as it is deliberately sacrificed and forced to corrode in order to prevent the iron or steel from doing so. As steel corrodes severely at potentials above -600 mV, the potential range necessary to protect steel in seawater is typically given as -850 mV to -1100 mV, though some sources give a higher maximum of -780 mV [4-7].

In the galvanic series, there are only three basic metals that are more active than steel: magnesium, zinc, and aluminum [3]. Magnesium has a very low working potential of about -1500 mV and is best

suited for high-resistance electrolytes but ill-suited to seawater [6]. Zinc has been used as a sacrificial anode for many decades, but it has certain drawbacks [8]. It has a fairly low current capacity (the amount of charge a metal can provide per unit mass) of 795 A-hr/kg, and it operates at a relatively low potential of -1040 mV [8]. Low potentials, starting below -800 mV but especially below -1000 mV, are known to generate large amounts of hydrogen and may cause embrittlement and stress corrosion cracking of steels [5].

Aluminum is an attractive alternative to zinc for use as a sacrificial anode. Aluminum has a much larger current capacity of 2974 A-hr/kg, and it can operate at higher potentials than zinc, -870 mV to -700 mV [5, 6]. Though the Hall-Héroult process for reducing aluminum metal from bauxite was patented in 1886, aluminum was not commercially available until the 1930s due to the large amounts of electricity consumed in the process [9]. Aluminum was first used as a battery anode in the Buff cell in 1857, but it was not used as a sacrificial anode until the early 1960s [10, 11]. The main issue with using aluminum as a sacrificial anode is that it forms a very stable and passive oxide layer, which prevents corrosion of the metal itself and limits the metal to a potential of -700 mV [6, 8].

In 1966, Reding and Newport published a study they had conducted wherein they surveyed roughly 2500 different alloys in order to study the effects of 37 different alloying elements, as single-, double-, and triple- element additions to aluminum. They found that many of the low-melting-point elements, such as Mg, Zn, Cd, Ga, In, Hg, and Sn, were able to disrupt the protective oxide and thus activate the aluminum such that it could corrode readily in seawater [6]. Reding and Newport patented an Al-Hg-Zn alloy [6], and in the same year, Sakano et al patented an Al-Zn-In alloy [12], which was the most widely used anode as of 2012 [8]. Figure 1 summarizes the potential range for protecting steel and where each of the metals and alloys that were discussed in this introduction lie on that range.

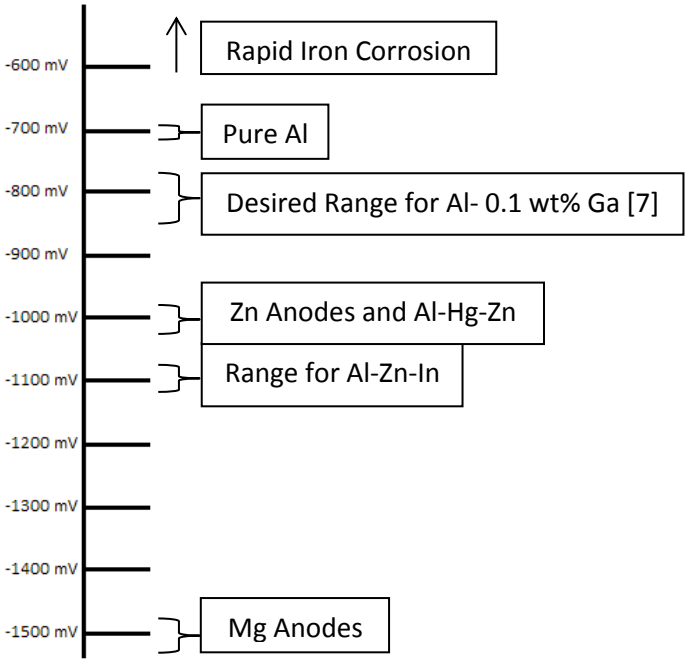

Figure 1: Potential Ranges for Zn, Mg, Al, Al-Ga, Al-Hg-Zn, and Al-Zn-In

The present work focused on understanding and characterizing the Al-Ga system, specifically Al-0.1 wt% Ga. Ga has relatively very high solubility in aluminum, up to ~20 wt% (9 at%) at the eutectic temperature of 26.6°C. Since the alloy of interest in this study contained 0.1 wt% Ga (~0.04 at%), the Ga should be fully in solution with no secondary phases. Figure 2 shows the Al-Ga binary phase diagram [13].

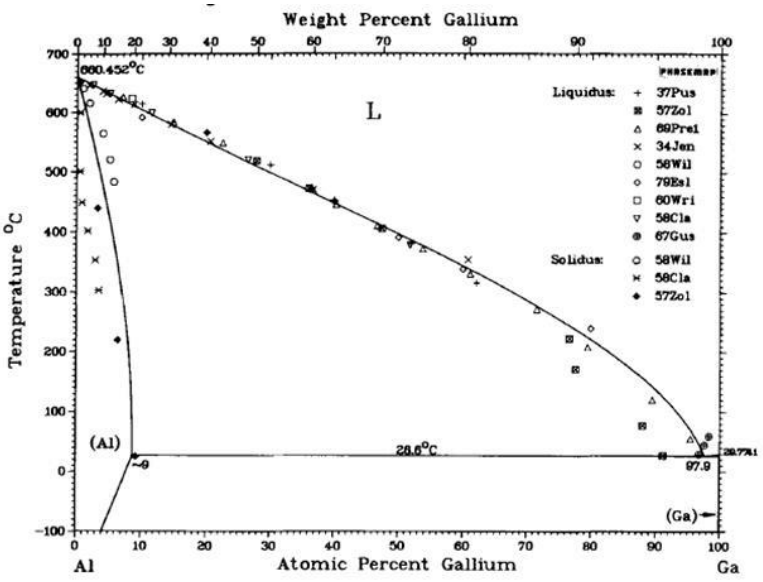

Figure 2: Al-Ga Phase diagram, from [13]. J. L. Murray, "The Al–Ga (Aluminum-Gallium) system," *Bulletin of Alloy Phase Diagrams,* vol. 4, pp. 183-190, 1983/09/01 1983. Used under fair use, 2015

1.3 Literature Survey of Aluminum-Gallium Activation Mechanisms

In 1976, Despic et al proposed that Ga can undergo reversible redox reactions at the metal-oxide interface, facilitating the movement of electrons between the two layers [4]. They also proposed a mechanism for Al dissolution in Al-Ga alloys, which is a fast electron transfer to form Al^{+}, followed by the rate-determining step: a slow simultaneous transfer of two electrons to form Al^{3+} [4]. In 1984, Reboul et al proposed that the Al-Ga anode dissolves, putting cations into the electrolyte. The Ga cations, being more noble than Al, would plate back onto the Al surface, causing local separation and thinning of the oxide layer [14]. They proposed that this deposition of activator metal was all that was necessary in order to activate the Al, and that all activators (Ga, In, Zn, etc) used this same mechanism [14].

In 1987, Tuck et al studied the Al-Ga system in both alkaline and chloride electrolytes [15]. They found that at Ga concentrations between 0.1 wt% and 2.6 wt%, they all quickly activated and reached a maximum current density, with increasing Ga content leading to shorter activation times [15]. In constant-current (galvanostatic) tests, they observed that prior to activation, the anodes exhibited uniform corrosion and that upon activation, pits of a uniform size distribution formed simultaneously, with no additional pits forming later [15]. They explained that the constant current fixed the amount of pit area that could corrode at any given time. Ga was found in high concentrations at the base of each pit. They proposed two mechanisms for the corrosion, one at open-circuit conditions and one under load. The open-circuit mechanism involved diffusion of Ga ions in the oxide to form discrete particles of Ga metal under the oxide film, causing localized film thinning [15]. As these particles grow, they can lead to swelling and eventual rupture of the oxide film, causing activation. The mechanism under load includes this film thinning and cracking, but it also includes a preferential dissolution of Al which leads to

further enrichment of surface Ga as discrete particles, as well as Ga ions that were dissolved into the electrolyte redepositing onto the top of the oxide layer [15], which is consistent with Reboul et al's model [14].

Both of these mechanisms, but especially the mechanism under load, depend on obtaining a critical surface concentration of Ga [15]. The surface Ga content of each anode over time was dependent on three processes: 1) the dissolution of the alloy into the electrolyte, 2) the dissolution of the gallium remaining on the anode after the first process, and 3) the back diffusion of the surface Ga into the alloy bulk [15]. They found that extended corrosion led to surface Ga accumulation which then diffused back into the alloy via grain boundaries, leaving Ga only on top of the oxide layer. Furthermore, in higher-Ga-content alloys, subsurface pits were observed after the oxide film had fallen off around them [15]. Lastly, they found that active alloys could be deactivated by cooling them from 60°C to 20°C. Tuck et al suggested that this behavior, coupled with the rapid diffusion of Al through the Ga particles, indicated that the Ga was in a liquid state when it activated the Al [15].

Breslin et al (1992) showed that polarization at -2000 mV dissolved Ga, producing hydrolysed oxides such as $HGaO_3^{2-}$, GaO_3^{3-}, and GaO_2^-, which could redeposit locally, enriching the surface with Ga. They proposed that this Ga enrichment "biased the surface charge towards activation", with a critical surface bias needed for full activation [16]. This surface bias increased chloride adsorption, which was a key aspect of the oxide breakdown in seawater and NaCl electrolytes [16]. With the film locally destabilized, there was competition between the processes of repassivation, which is the formation of a new, stable oxide layer, and dissolution, with fluctuations in measured potential occurring due to the nucleation, growth, and death of pits [16]. This nucleation-growth-death mechanism for pits was modeled in 2013 by Murer et al for Al 2024 alloys using a deterministic Monte Carlo approach, with good agreement between mathematical predictions and their collected experimental data [17]. Breslin et al's findings help to support Tuck et al's mechanism for activation under load. However, Breslin et al also found that Al cannot be activated solely by Ga^{3+} in solution; there has to be some amount of Ga in solid solution within the anode itself in order to activate via Ga^{3+} deposition [16]. This contradicted Reboul et al's proposal that activator ions in the electrolyte were the sole cause of activation.

In 1992, Carroll et al found that Ga^{3+} ions in the electrolyte dramatically reduced the potential range for passive behavior of Al-Ga alloys, both increasing the open circuit potential (from -1500 mV to -1050 mV) and reducing the transpassive potential (from -700 mV to -1000 mV) [18]. This was likely due to Ga ions depositing onto the surface of the anode, which is consistent with both Tuck et al's models and that of Reboul et al.

Textor et al, in 1994, found an enrichment of Ga about 1-2 nm below the oxide-metal interface in an Al-0.5 wt% Mg-0.0085 wt% Ga alloy, which peaked at about 2 at% Ga [19]. Higher Ga surface concentrations also led to lower open circuit potentials in 1M NaCl, from -810 mV with 1.7 at% Ga to -1100 mV with 7.8 at% Ga [19].

In 2000, Margadant et al found that microscopic voids can form underneath the oxide layer of Al-Ga; they were caused by local oxidation of Ga particles, since the Pilling-Bedworth Ratio, the ratio of oxide volume to metal volume, for Ga is about 25% lower than that of Al [20].

In 1997, Aragon et al showed that liquid Ga can easily supercool below its normal melting point of 29°C (supporting Tuck et al's hypothesis that the Ga was liquid), and that the presence of liquid Ga on the surface of Al causes increased depassivation of the Al [21]. Ashitaka et al [22] found in 2002 that sufficient enrichment of Ga underneath the oxide layer of Al can cause detachment of the oxide, exposing the bare Al; this is congruent with Margadant et al's finding.

Flamini et al's work in 2006-2008 proposed an addition to the mechanism for how Ga activates Al [23-25]. Preferential dissolution of Al leads to surface enrichment of Ga. Once a critical concentration of Ga has been reached, a liquid Ga-Al amalgam forms and spreads across the anode, detaching and thinning the oxide film. This amalgam provides fairly rapid transport of Al from the bulk-amalgam interface to the amalgam-electrolyte interface in a diffusion-controlled process, as in Tuck et al's models. This amalgam is maintained by the highly exothermic oxidation of Al to Al^{3+} (ΔH^0 = -1406 kcal/mol). The endothermic Ga melting reaction was not discussed. Ga is also dissolving and redepositing on the oxide surface; this, combined with the limitation on Al diffusion through the amalgam, causes the amalgam to become saturated with Al and thus slows the corrosion rate. Because the amalgam is sustained by the exothermic dissolution of Al, there is a minimum corrosion rate necessary to maintain the amalgam, as found by Senel et al [26]. As the reaction slows, the amalgam is no longer sustained and it solidifies, effectively repassivating the anode without the presence of another mechanism. However, in chloride-rich environments, such as seawater, the Ga that deposited on the surface, as well as the solid amalgam itself, facilitates chloride adsorption on the surface of the anode, causing pitting to occur. Ga alone can activate Al in this way if given enough time; Zn and/or Sn in the alloy can greatly reduce the time needed for activation by increasing Ga wetting and Ga^{3+} deposition [24, 27]. This mechanism is supported by the work of Textor et al [19], Aragon et al [21], and Ashitaka et al [22].

1.4 Summary of Proposed Activation Mechanisms

Because Reboul et al's activator-deposition-only mechanism was refuted by Breslin et al, there are currently two prevailing mechanisms for the activation of Al by Ga, the first by Tuck et al [15], and the modification by Flamini et al [23-25]. The mechanisms that are considered in this thesis are 1) Tuck et al's discrete-particle mechanism [15] and 2) Flamini et al's amalgam-layer mechanism [23-25]. The discrete-particle mechanism consists of the following steps:

- Preferential dissolution of Al leads to Ga enrichment under the oxide film
- Ga both under the oxide agglomerates as discrete particles
- Ga dissolved in the oxide diffuses to these particles, thinning the oxide
- Since Ga can be easily supercooled below its melting point of 26.6°C, the particles may be liquid at the test temperature (~25°C)
- As these particles grow, they cause swelling under the oxide
- A critical concentration of Ga causes cracking of the oxide, exposing the particles directly to the electrolyte
- The liquid particles provide rapid transport of Al from the bulk metal to the electrolyte
- Ga enhances chloride adsorption at these sites, causing pitting
- Partial Ga dissolution leads to Ga metal depositing on top of oxide film
- These Ga deposits also lead to pitting by chloride adsorption

- Some Ga diffuses back into the alloy via surface and grain boundary diffusion, leading to a steady-state Ga surface content

Figure 3 shows a schematic diagram of Tuck et al's discrete-particle mechanism [15].

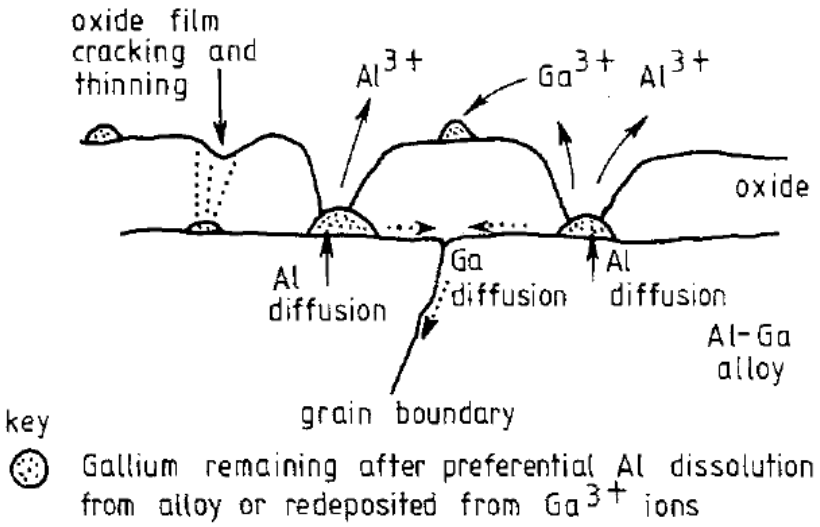

Figure 3: Schematic diagram of Tuck et al's discrete-particle mechanism, from [15]. C. Tuck, J. Hunter, and G. Scamans, "The Electrochemical Behavior of Al-Ga Alloys in Alkaline and Neutral Electrolytes," *Journal of the Electrochemical Society,* vol. 134, pp. 2970-2981, 1987. Used under fair use, 2015

The amalgam-layer mechanism adds an additional stage to activation [23-25]:

- Preferential dissolution of Al leads to Ga enrichment under the oxide film
- Once sufficient Ga enrichment has been achieved, a stable liquid Ga-Al amalgam forms and spreads under the oxide film
- This amalgam detaches the oxide film, exposing the amalgam directly to electrolyte
- The amalgam provides rapid transport of Al from the bulk metal to the electrolyte, causing uniform corrosion over a large area at potentials around -1500 mV
- The amalgam is maintained as a liquid by the exothermic dissolution of Al
- Ga partially dissolves and Ga^{3+} deposits on top of the aluminum oxide, and the amalgam saturates with Al, slowing the reaction
- As the reaction slows, the amalgam solidifies, repassivating the anode unless in the presence of chlorides
- Ga that deposited on the oxide increases adsorption of chlorides, causing activation via pitting at potentials around -1100 mV

The two mechanisms share many similarities: they both involve preferential dissolution of Al, require a critical surface concentration of Ga, involve Ga deposition on top of the aluminum oxide, and ultimately lead to pitting. The key difference between them is that the discrete-particle mechanism keeps the liquid Ga as particles that locally disrupt the oxide and directly lead to pitting, whereas the amalgam-layer mechanism allows the liquid Ga to spread across the surface of the metal and cause uniform corrosion before solidifying and causing pitting.

1.5 Previous Studies at Virginia Tech

Previous work on Al-0.1 wt% Ga at Virginia Tech made master heats of Al-0.1 wt% Ga and took the master heat and remelted it in order to make ternary alloys, such as Al-Ga-Cu or Al-Ga-Si [28]. It was found that the Al-Ga master heat was typically poorly-behaved and gave inconsistent results, while the alloys produced from remelting the master heat were typically well-behaved. This erratic behavior is not reported in the public domain; few articles, if any, discuss the repeatability of electrochemical corrosion tests on Al-Ga. This study aimed to characterize and understand the effects of remelting on the performance of Al-0.1 wt% Ga.

2. Methods

A wooden pattern was used to produce nobake sand molds that produced four plates approximately 3.5” x 3.5” x 0.25”. The binder used for the sand was a two-part system consisting of Phenoset RB and APR-015. The cope mold consisted of a solid block of bonded sand approximately 2” thick with two 1” diameter holes drilled through it, each lining up with the well in the drag. On top of the cope, additional blocks of sand, one for each downsprue, had 1” diameter holes drilled through them to lengthen the downsprue and the top of each cup was filed by hand to widen the opening. These blocks were attached to the cope using core paste. Figure 4 shows the wooden pattern used to make the sand molds.

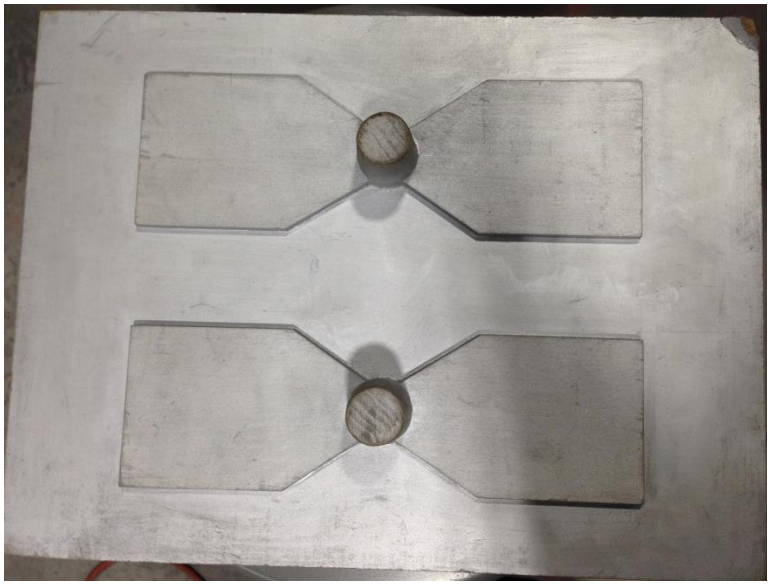

Figure 4: Wooden pattern used to make nobake sand molds, with two wells and four plates in each mold.

Three heats of Al-0.1 wt% Ga were studied in this thesis: a master heat and two remelts. The master heat was made fresh, and was not the master heat used in previous studies. The master heat was produced by melting 26.6 lbs of 99.99% Al (supplied by Milward Alloys) and adding 0.1 wt% (0.027 lbs) of 99.99% Ga (supplied by Rotometals) in a #30 SiC crucible using an Inductotherm lift-swing induction furnace. It was poured into four of the plate molds (16 plates total) and the remainder was poured into ingot molds. The molds were left to sit for an hour, at which point they were opened to allow for faster cooling. Once at room temperature, the plates and ingots were grit-blasted using alumina particles to remove surface sand picked up during casting. The plates were cut from the downsprues and cut into 4 samples each, approximately 1.5” x 1.5” x 0.25”. The downsprues and ingots, weighing 21.8 lbs, were then put back into the crucible and melted again to make the 1st remelt. This was poured into two plate molds (8 plates) and the rest into ingots, which were given the same cooling, grit-blasting, and cutting treatment as the master heat. The downsprues and ingots, weighing 18.8 lbs, were then melted again in the same fashion to make the 2nd remelt. This was also poured into two plate molds and the rest into ingots. The plates were given the same treatment as the previous heats.

For each heat, a spectrometer sample was poured using a steel mold, and analyzed on a Bruker Q4 Tasman Optical Emission Spectrometer at the Virginia Tech foundry.

For corrosion tests, each sample was first ground on both sides using 80 grit SiC abrasive paper to remove the exterior as-cast surface and produce a flat sample. Then the samples were ground on one side only, using successive grits of 240, 320, 400, then 600 SiC wet/dry abrasive paper under running water. After the final grinding step, each sample was rinsed with 200 proof ethanol and quickly dried using a heat gun set to low. The samples were not ground to 600 grit until just before setting up corrosion tests. X-ray photoelectron spectroscopy (XPS) samples were further ground to 1000 grit and then ultrasonically cleaned for five minutes while submerged in 200 proof ethanol.

Corrosion tests were performed using a Princeton Applied Research 4-channel Versastat MC in a Model K0235 Flat Cell, Figure 5, which exposed a constant area on each sample, 1 cm^2. The counter electrode for all tests except galvanic coupling was a platinum mesh. The counter electrode for galvanic coupling was a 1" x 1" x 0.5" square of 1123 steel (supplied by Metalsa), ground to 600 grit using the same methods described above. The reference electrode for each test was a saturated KCl calomel electrode (SCE). The electrolyte used for all testing was pre-prepared ASTM D1141 synthetic seawater [29] supplied by Cole Parmer. The tests were all run in accordance with ASTM G1 [30], G5 [31], and G69 [32]. All samples were tested in the as-cast state, except for those used in a heat treatment study, in section 3.7 of this thesis. The samples in the heat treatment study were taken from a previous master heat from July 2014 and given two different treatments: solutionized at 538°C for one hour followed by a water quench, and aged at 121°C for 24 hours followed by air cooling.

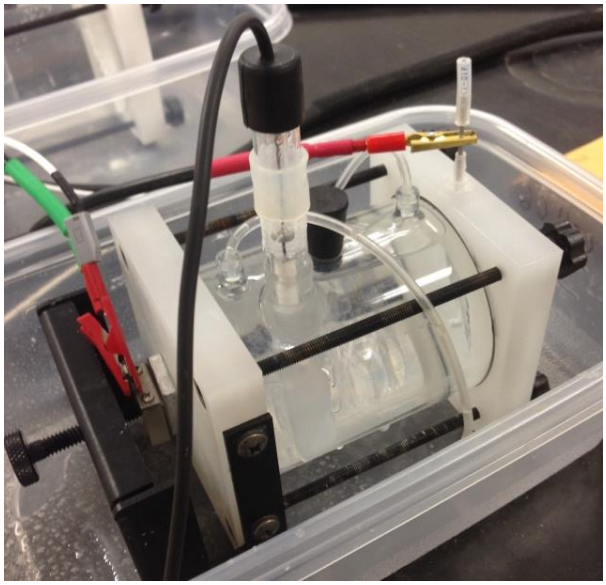

Figure 5: Flat Cell Test Setup

Scanning electron microscope (SEM) and energy-dispersive x-ray spectroscopy (EDS) analysis was performed using the FEI Quanta 600 FEG Environmental Scanning Electron Microscope with attached Bruker Quantax 400 EDS at Virginia Tech's Nanoscale Characterization and Fabrication Laboratory (NCFL). All SEM images in this thesis were taken using the secondary electron detector. XPS analysis was carried out using a PHI Quantera XPS, also at NCFL. The sputtering for XPS used Ar^+ ions.

3. Results and Discussion

3.1 Spectrometry

The three heats did not have significantly differing chemical compositions, as would be expected, since they were all melted from the same materials. Unfortunately, the spectrometer at the VT foundry was unable to read Ga contents greater than 0.048 wt% (target Ga content for the master heat was 0.1 wt% Ga), so we were unable to see if the Ga content changed across the three heats. The impurities seen in the spectrometer results are most likely due to leftover residues in the instrument (especially Si, Fe, and Cu), as later XPS analysis shows the absence of any elements in the samples except Al, O, and Ga. The results are summarized in Table 1.

Table 1: Optical Emission Spectrometer Results, in averaged wt%

	Si	Fe	Cu	In	Zn	Hg	Bi	Sn	Ga	Al
Low-Voltage Specification [7]	<0.10	<0.08	<0.005	<0.005	<0.15	<0.005	N/A	<0.001	0.092-0.110	Bal
Master Heat	.0076	.0092	.047	<0.002	<0.002	<0.002	<0.003	<0.002	>.048	Bal
1st Remelt	.0078	<.0020	.025	<0.002	<0.002	<0.002	<0.003	<0.002	>.048	Bal
2nd Remelt	.0085	<.0020	.028	<0.002	<0.002	<0.002	<0.003	<0.002	>.048	Bal

3.2 Open Circuit

Open circuit potentials (OCPs) were measured by creating an electrical circuit, in the flat cell, between the sample and a platinum counter electrode, but not impressing any current or potential. Data was collected for 240 hours for each sample, recording one data point every five minutes. The Versastat software used to control the corrosion testing equipment also recorded the initial OCP immediately when the test begun. The initial potentials started off somewhat high and wide-ranging between the three heats, but they eventually fell and leveled out to approximately the same value after approximately three days. All three heats maintained a steady potential for two to three days. Towards the end of the test, the 2nd remelt OCP began to slowly rise again. Table 2 shows the starting OCP, the potential after five minutes (the first data point) and the average potential of the last 24 hours for each heat. Figure 6 shows the results graphically. Since the OCP of the second remelt started to drift higher towards the end of the test, the average is seen to be somewhat higher than the rest. The average of the time when it was virtually flat (from hours 100 to 160) was -1530 mV.

Table 2: Open Circuit Potentials over time

Heat	Starting OCP (mV)	OCP after 5 minutes (mV)	Last 24 hours Average OCP (mV)
Master Heat	-1158	-1154	-1541
1st Remelt	-837	-836	-1530
2nd Remelt	-1031	-1025	-1479

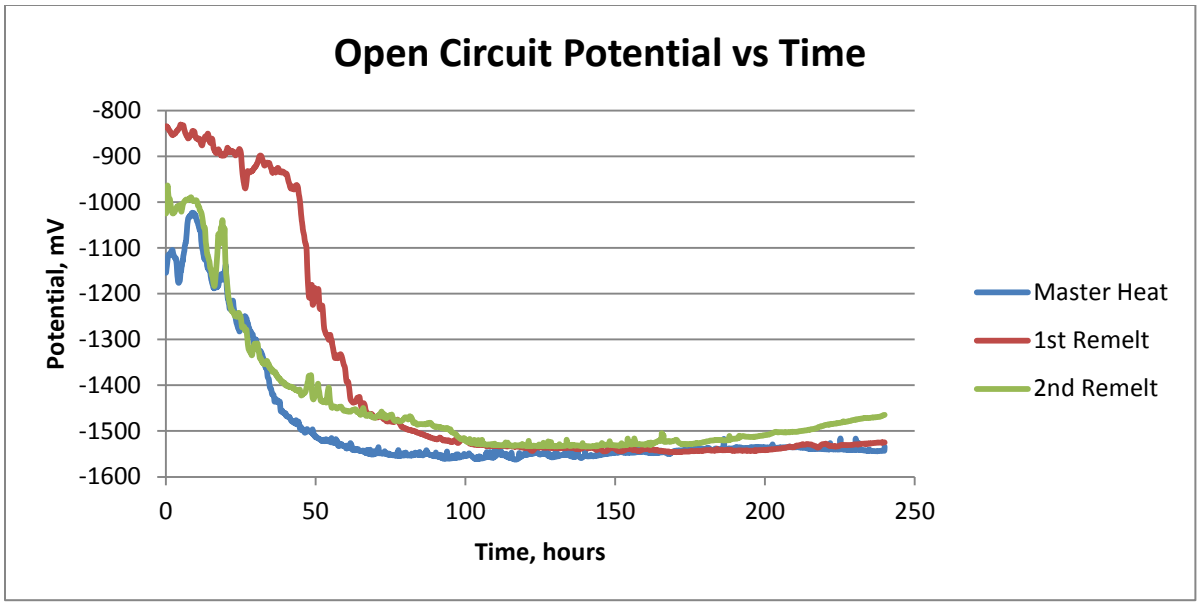

Figure 6: Open Circuit Potentials. All three heats took about 3 days to reach a steady state; two heats kept stable, one showed drifting

3.3 Galvanostatic

3.3.1 Prior work

Prior work at Virginia Tech performed galvanostatic tests at 9 A/m^2, which was the average current observed for non-polarized electrodes when coupled to steel in seawater by Pautasso et al [33].
To establish a baseline, pure Al samples were produced and tested; the data are shown in Figure 7. As expected, the pure Al was passive or possibly even transpassive, given the current density, and the sample had a high potential range of -700 to -720 mV.

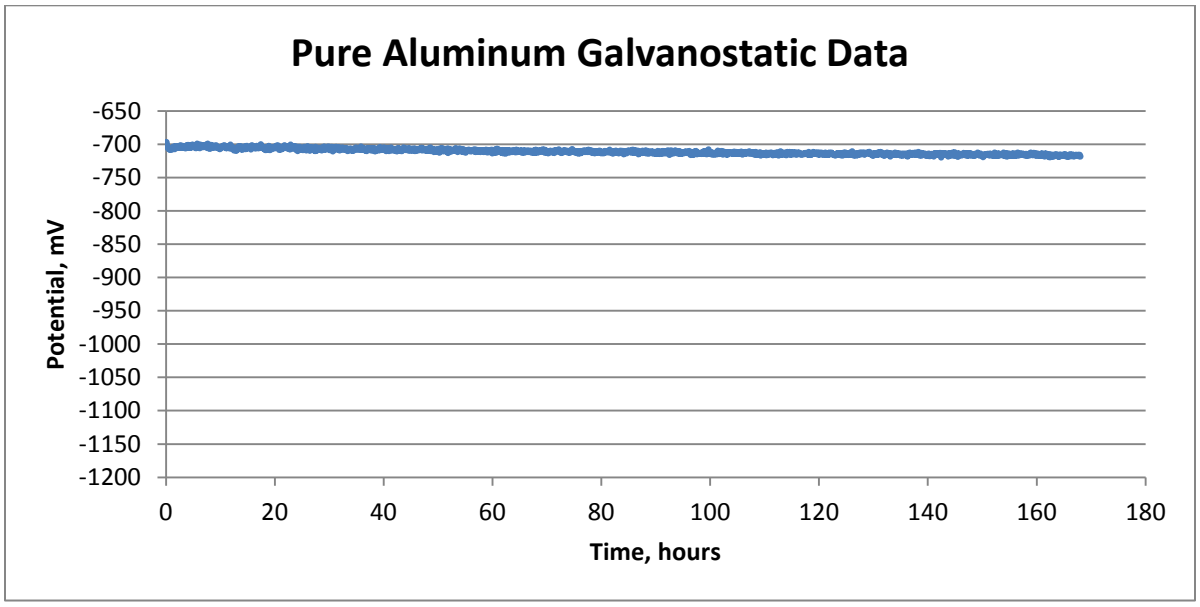

Figure 7: Pure Al galvanostatic data, with relatively noble potentials and slight decrease in potential at long times. Used with permission from Alan Druschitz, 2015.

As of 2012, the leading commercial Al anode was an Al-Zn-In alloy [8]. It was also tested as part of the prior work, and the data are shown in Figure 8. The alloy is quite active, achieving potentials at or below -1100 mV. This makes it an effective anode, but as discussed in the introduction, a low potential will generate large amounts of hydrogen, which may lead to embrittlement and stress corrosion cracking. Thus the Al-Zn-In alloy operates at too low of a potential to meet the low-voltage specification [7].

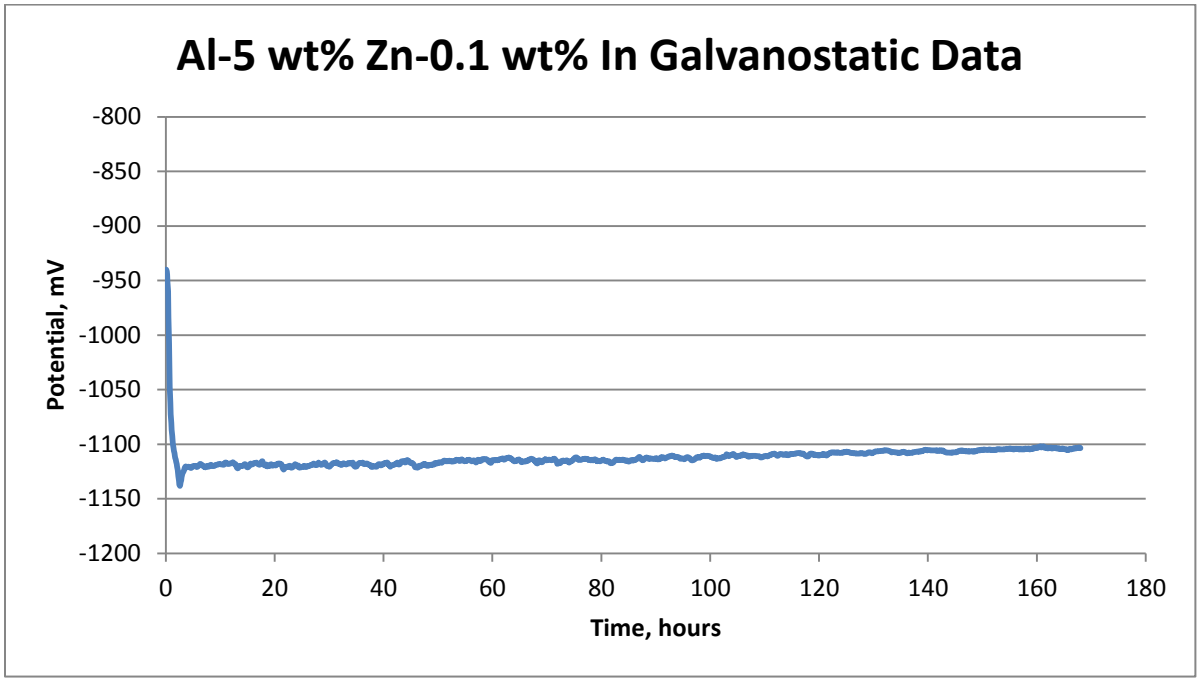

Figure 8: Al-5 wt% Zn-0.1 wt% In galvanostatic data, showing lower-than-desired steady-state potentials. Used with permission from Alan Druschitz, 2015

The prior work at Virginia Tech on Al-0.1 wt% Ga found that master heats displayed inconsistent performance while the alloys made from remelting the master heats exhibited less test-to-test variation. Figure 9 shows a galvanostatic run for the first Al-0.1 wt% Ga heat, tested in October 2013. The October master heat was very well-behaved, quickly reaching a potential of -811 mV in about 2 hours, then more slowly reaching -833 mV after about 20 hours. The potential stayed there until about the 42-hour mark, where it started to very slowly and linearly decrease in potential, reaching a final value of about -843 mV after 168 hours. This potential was within the desired potential range for protecting steel [5].

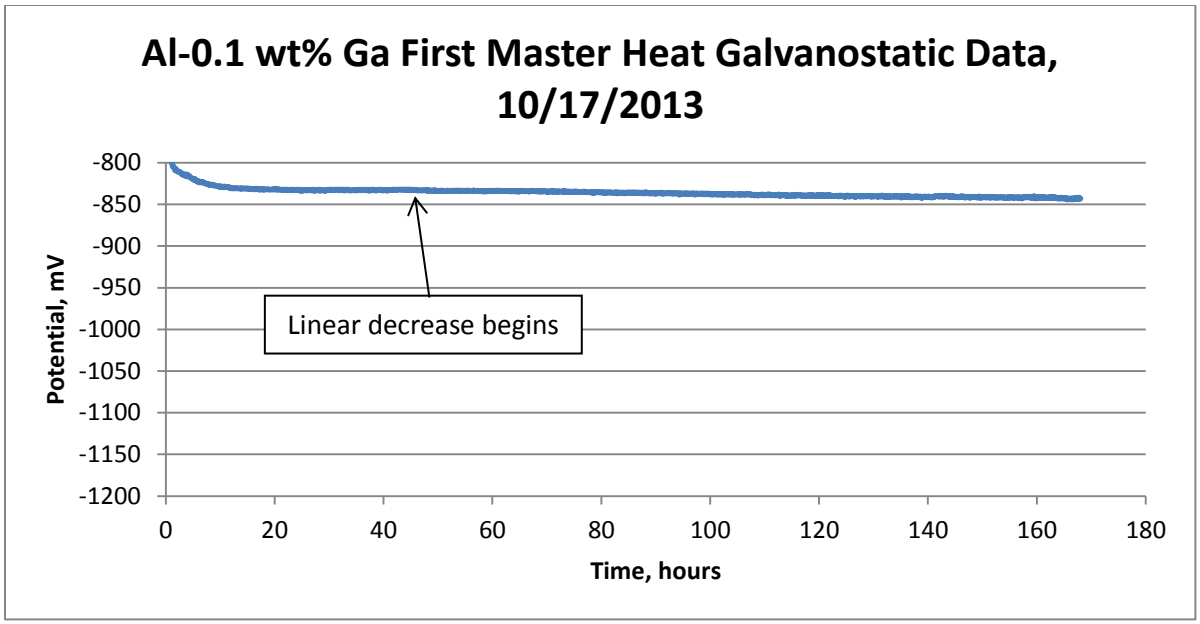

Figure 9: October Al-0.1 wt% Ga master heat galvanostatic data, showing steady behavior. Used with permission from Alan Druschitz, 2015

Figure 10 shows another master heat, made and tested in July 2014, which exhibited very different behavior compared to the first master heat from October 2013. Within an hour and a half it reached -810 mV and the started to slowly decrease. At about 3 hours, the potential suddenly decreased to -830 mV and started to fluctuate. At about 11.5 hours, the potential decreased towards -950 mV, finally moving into a range between -1050 mV and -1150 mV, which is similar to that of the Al-Zn-In anode from Figure 8 and thus lower than the desired potential. This potential range was centered around -1100 mV, which is the pitting potential described in the amalgam-layer mechanism.

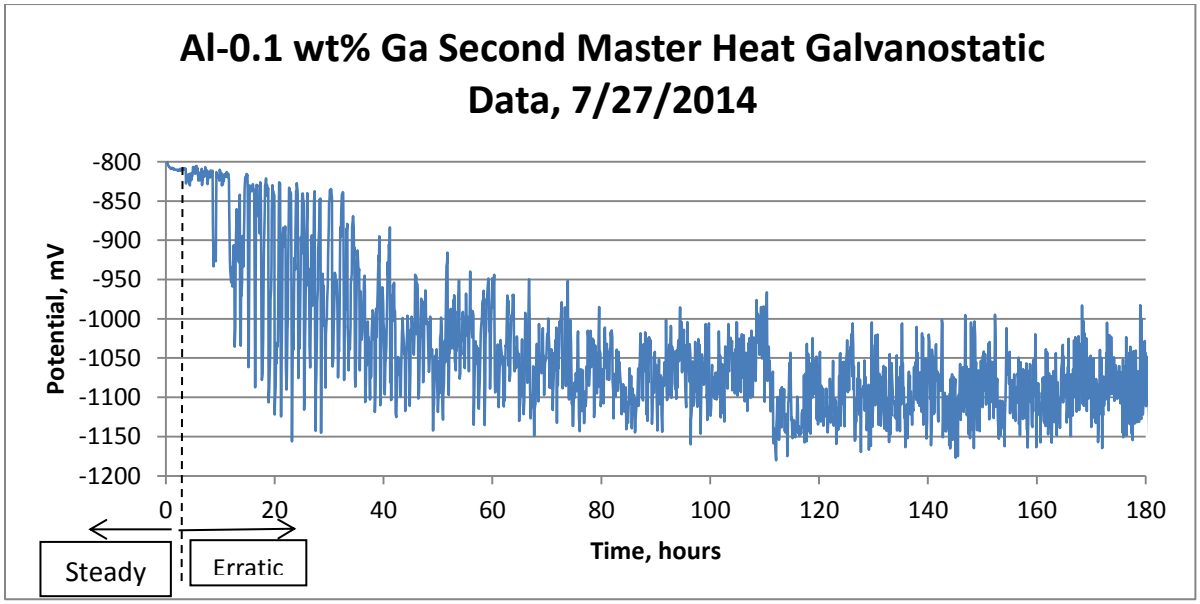

Figure 10: Second Al-Ga Master Heat galvanostatic data, showing inconsistent behavior after about three hours of testing. Used with permission from Alan Druschitz, 2015

Figure 11 shows three different alloys made by remelting the Al-Ga master heats [28]. The Cu alloy was made from the October master heat and the Si and Ge alloys were made from the July master heat. All three of the alloys are very similar, with steadily-decreasing potential through the entire 168 hours of the test.

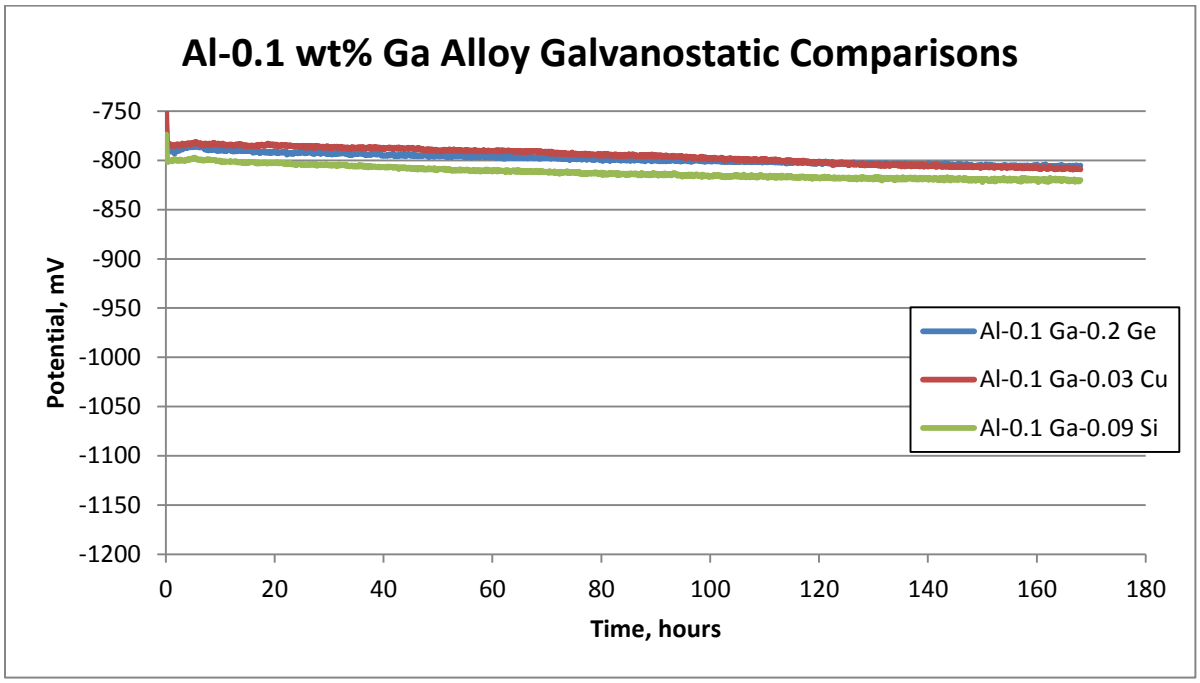

Figure 11: Galvanostatic data for Al-Ga Alloys from remelted master heats, showing consistent behavior. Used with permission from Alan Druschitz, 2015

3.3.2 Current Work

The master heat produced for this study exhibited very similar behavior to that of the July 2014 master heat. Galvanostatic tests were performed at 6.2 A/m^2, as per the NACE standard for testing aluminum anodes [34]. On both runs, the potential quickly reached ~-815 mV and held steady for a short time, but spiked downwards and began fluctuating after 2-3 hours, increasing in amplitude until roughly the 30-hour mark. These fluctuations are likely due to pitting. Galvanostatic test data for the Al-0.1 wt% Ga master heat produced for this study is shown in Figure 12.

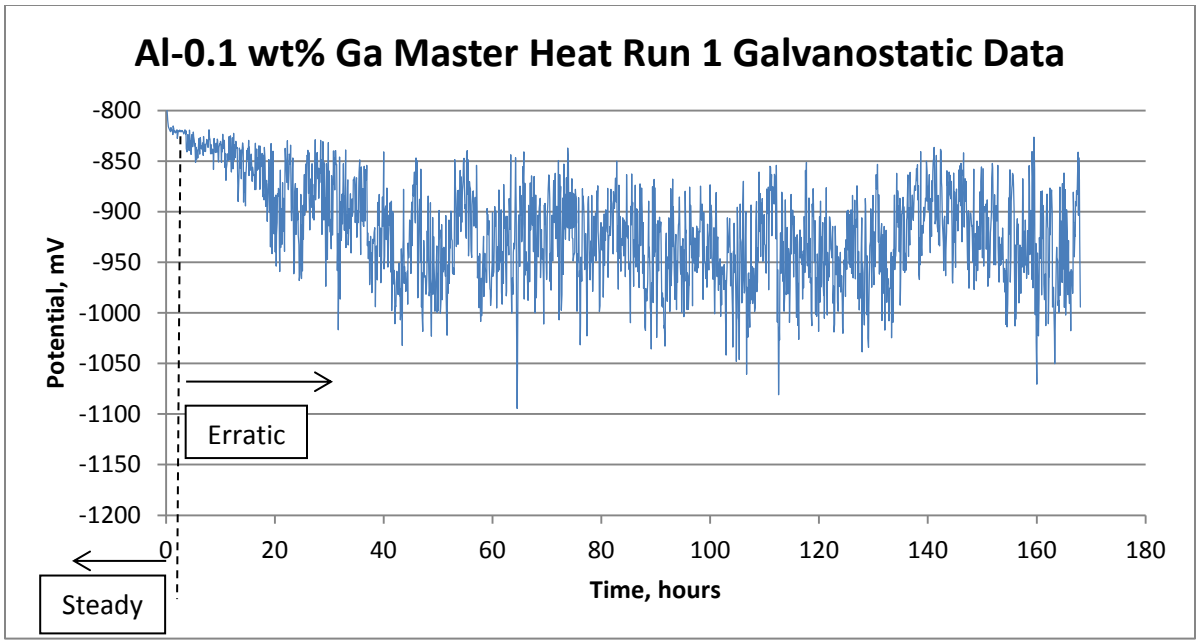

Figure 12: Al-0.1 wt% Ga Master Heat run 1 galvanostatic test data, showing fluctuations in potential

The 1st remelt exhibited somewhat similar behavior in galvanostatic tests, but held a steady potential for much longer (30-50 hours) than the master heat. Galvanostatic test data for the Al-0.1 wt% Ga 1st remelt produced for this study is shown in Figure 13.

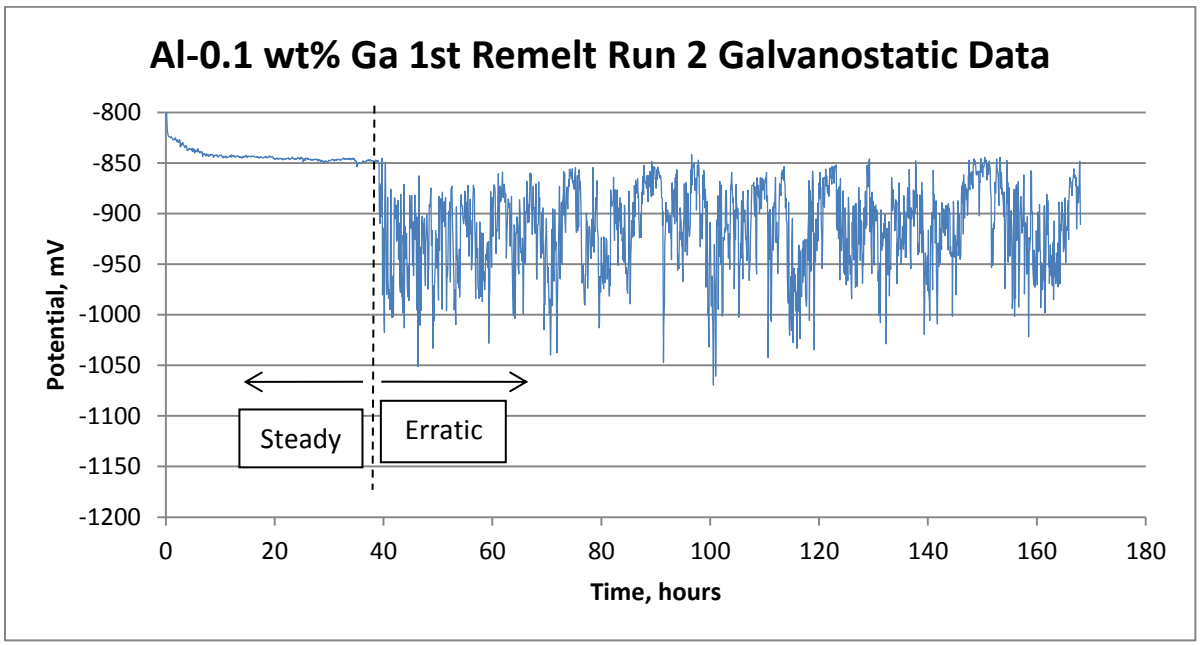

Figure 13: Al-0.1 wt% Ga 1st Remelt run 2 galvanostatic test data, showing longer steady behavior than master heat

The 2nd remelt had similar behavior to that of the 1st remelt, but the length of time that the 2nd remelt held a steady potential was inconsistent, ranging from 6 hours to 540. As seen in Figure 14, the first run, which lasted the longest, maintained a steady potential until the 90-hour mark, at which point it slowly and linearly decreased in potential, much like the behavior of the alloys seen in prior work.

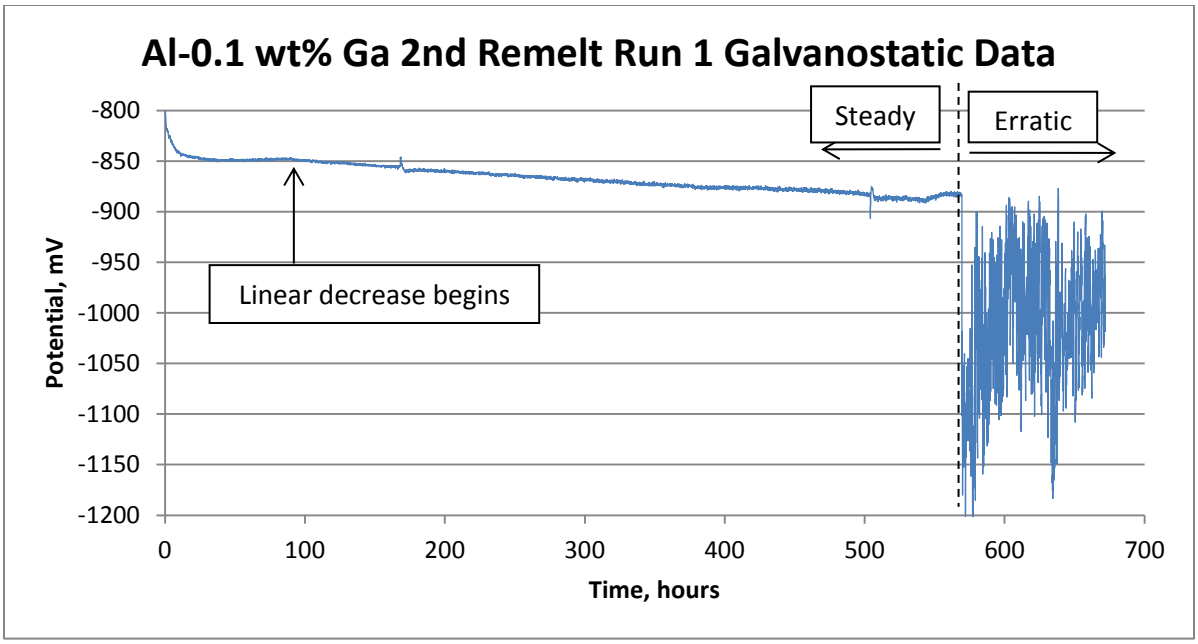

Figure 14: Al-0.1 wt% Ga 2nd Remelt Run 1 galvanostatic test data, showing longer steady behavior and linear decrease

Clearly the remelting process altered the behavior of these alloys and extended the length of time needed for the alloy to exhibit erratic behavior.

Further comparison of the galvanostatic data is shown in Table 3. "Steady Start" is the time of the first point that is within the rest of the steady potential range. "Last Steady" is the time of the last point in the steady range before a sharp decrease that does not return to the steady range. "Steady Time" is the length of that steady potential plateau. Average potentials and standard deviations are also calculated for both the steady and erratic regions of each run. In all cases, the erratic regions were at much lower potentials and had much more variation than the steady regions. The 2nd remelt had inconsistent steady times, but all of them were still longer than those of the master heat tests. Both the remelts had longer steady times than the master heat, but there is less of a clear difference between the two remelts. The remelts also had similar steady potentials, all of which were higher than those of the master heat.

Table 3: Galvanostatic Summary with Steady Plateau times and average potentials

Heat	Run	Steady Start (s)	Last Steady (s)	Steady Time (s)	Steady Time (h)	Steady Average E (mV)	Steady σ (mV)	Erratic Average E (mV)	Erratic σ (mV)
Master Heat	1	1,500	13,200	11,700	3.25	-820.1	2.2	-930	48.5
	2	2,100	11,400	9,300	2.58	-806.8	1.1	-912	45.8
1st Remelt	1	30,300	229,500	199,200	55.3	-835.0	5.4	-914.9	47.7
	2	27,300	140,100	112,800	31.3	-845.5	2.1	-914.8	41.8
2nd Remelt	1	115,500	2,255,400	1,934,400	537.3	-848.5	0.7	-1004.7	64.3
	2	36,300	139,200	102,900	28.6	-848.5	3.7	-943.4	44.9
	3	21,300	77,100	55,800	15.5	-837.6	2.1	-904.3	40.2
	4	1,200	23,400	22,200	6.2	-835.0	6.8	-978.1	35.6

3.3.3 Corroded Microstructures

In all samples observed after becoming erratic in galvanostatic tests, there was pitting observed on the exposed surface, most notably in a large and broad pit located at the base of the sample. This may be evidence of crevice corrosion, which would be an artifact of the testing setup. The flat cell uses a teflon O-ring to create a water-tight and corrosion-immune seal between the cell and the sample, but that O-ring creates a sharp 90° angle where it contacts the sample, so that may be an area of increased chance of crevice corrosion. Regardless, this artifact would affect all samples the same, so the fact remains that differences in behavior have been consistently seen between the different heats. Aside from the large pit at the base of each sample, all samples also had pits at the O-ring interface and underneath it, for the aforementioned reasons. The roughness of the samples (600 grit, or 10.6 µm) may have allowed some electrolyte to penetrate underneath the O-ring and cause crevice corrosion. Large amounts of light-colored deposits can be seen on nearly every sample; these were salt deposits, residue from the synthetic seawater, as well as some possible aluminum-based corrosion products. Figures 15 through 18 show various features of the master heat galvanostatic corrosion, with pitting all across the exposed surface, including some with a cracked-mud appearance, indicating corrosion underneath the oxide film, causing thinning and cracking. The cracked-mud appearance in Figure 17 supports the discrete-particle mechanism. The lack of observed uniform corrosion does not support the amalgam-layer mechanism.

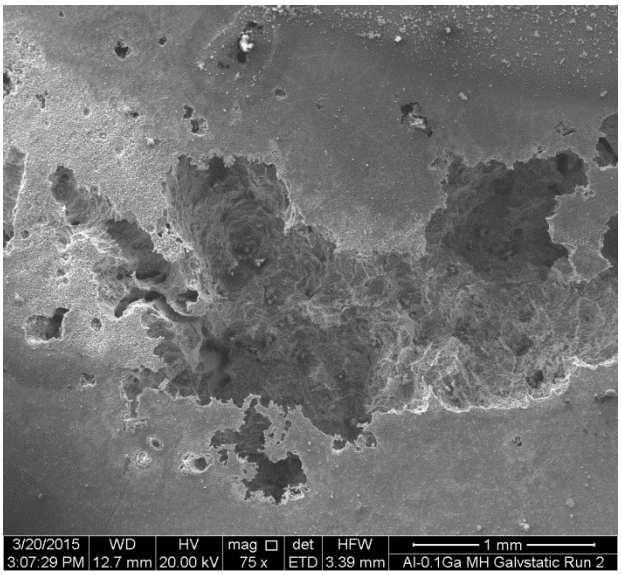

Figure 15: SEM image of master heat after galvanostatic testing, showing large, heavily corroded area at base

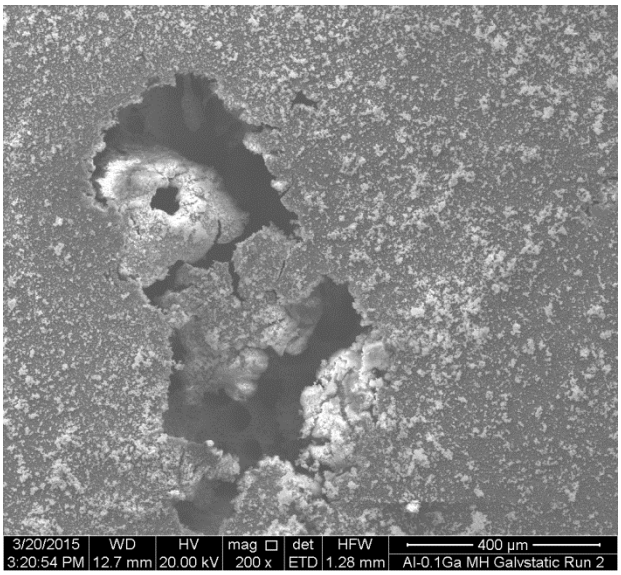

Figure 16: SEM image of master heat after galvanostatic testing, showing a typical large pit with additional attack below sample surface

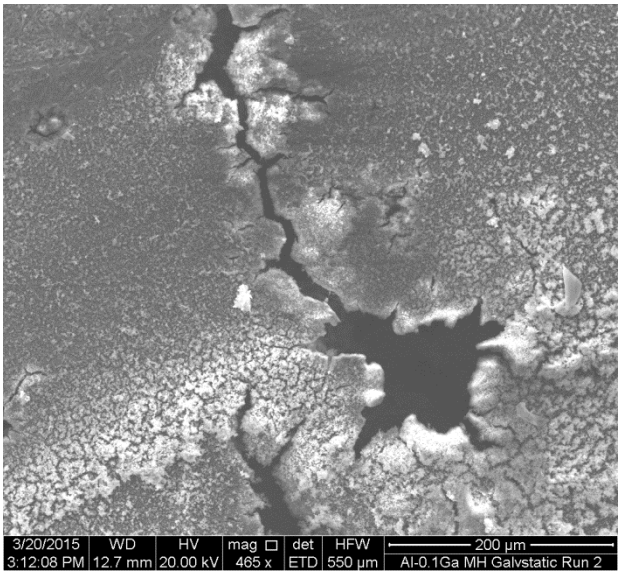

Figure 17: SEM image of master heat after galvanostatic testing, showing a cracked-mud pit, which indicates local attack under the oxide

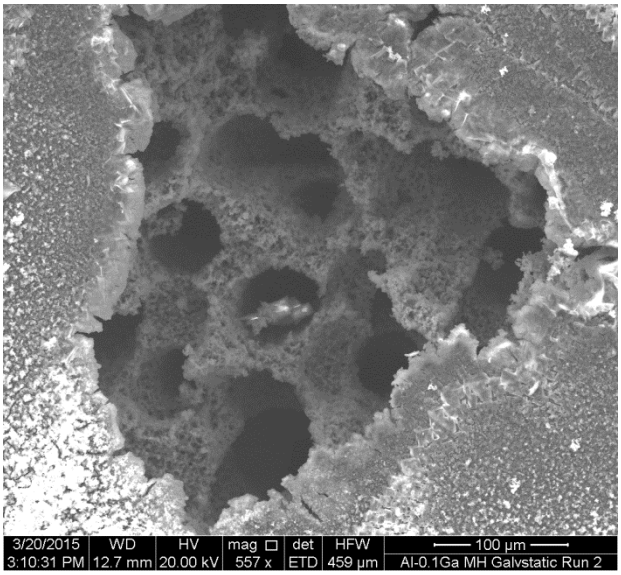

Figure 18: SEM image of master heat after galvanostatic testing, showing the presence of multiple pits forming at the same location

Figures 19 and 20 are SEM images of the first remelt after galvanostatic testing, showing the relative lack of pits on the exposed surface (the large pit at the base is still present) Pits under the O ring are present.

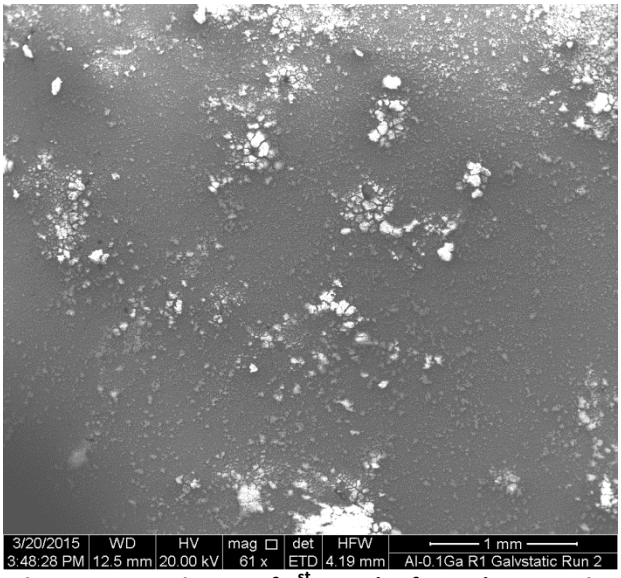

Figure 19: SEM image of 1st remelt after galvanostatic testing, showing general exposed surface with many deposits but fewer pits

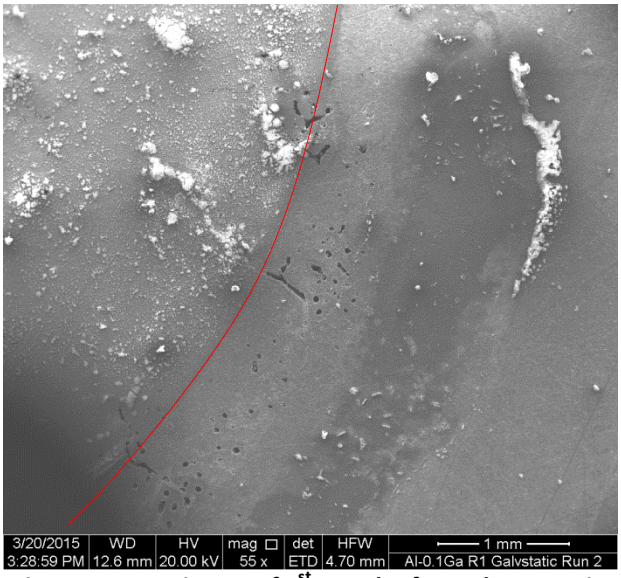

Figure 20: SEM image of 1st remelt after galvanostatic testing, showing pits under the O-ring. The O-ring interface is highlighted in red.

Figures 21 and 22 are SEM images of the second remelt after galvanostatic testing, which remained steady for 29 hours, exhibiting similar behavior to the first remelt.

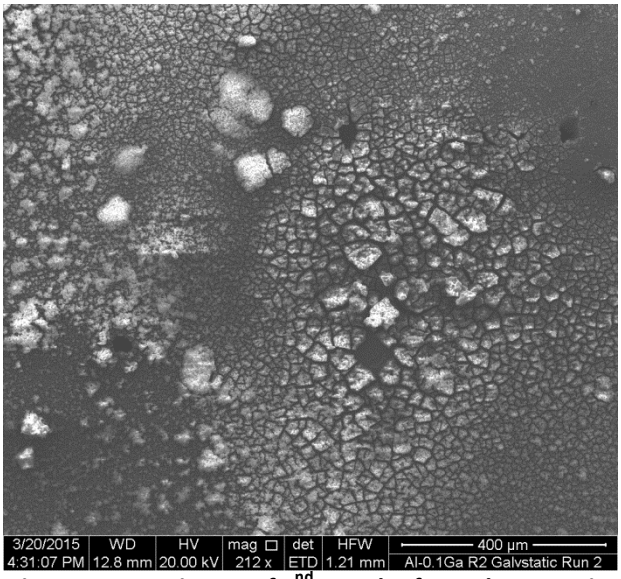

Figure 21: SEM image of 2nd remelt after galvanostatic testing, showing general surface with few pits

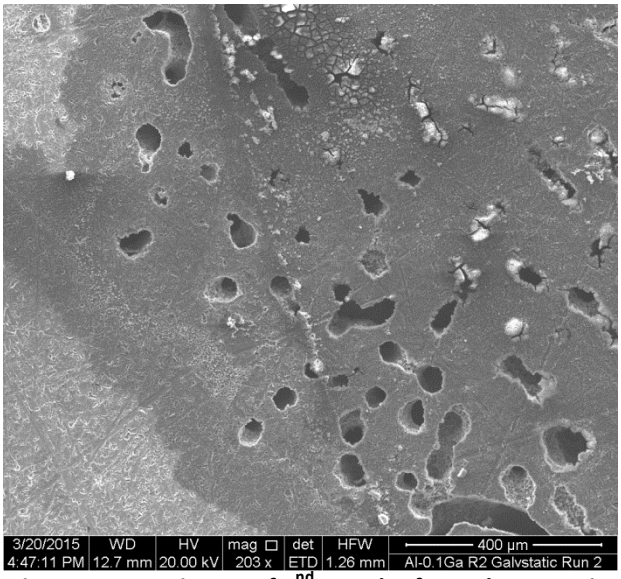

Figure 22: SEM image of 2nd remelt after galvanostatic testing, showing pits under O-ring, which are evidence of crevice corrosion

Figures 23 through 26 are SEM images of the second remelt run 1 after galvanostatic testing, which ran for 537 hours. The images show pitting across the surface, as would be expected of a sample that became erratic at such high potentials, but they also reveal a difference in the large corroded area at the base of the sample. Instead of a broad crater, as seen in Figure 15, there were columns of metal left behind, which indicate more localized attack.

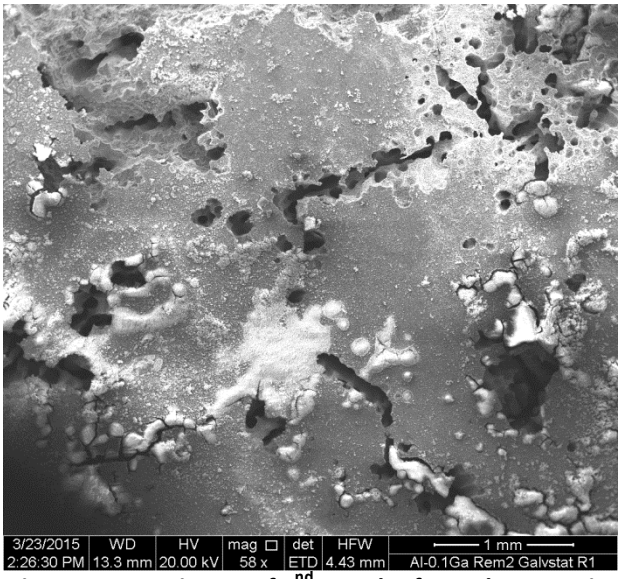

Figure 23: SEM image of 2nd remelt after galvanostatic testing, showing general exposed surface with numerous pits across the sample surface

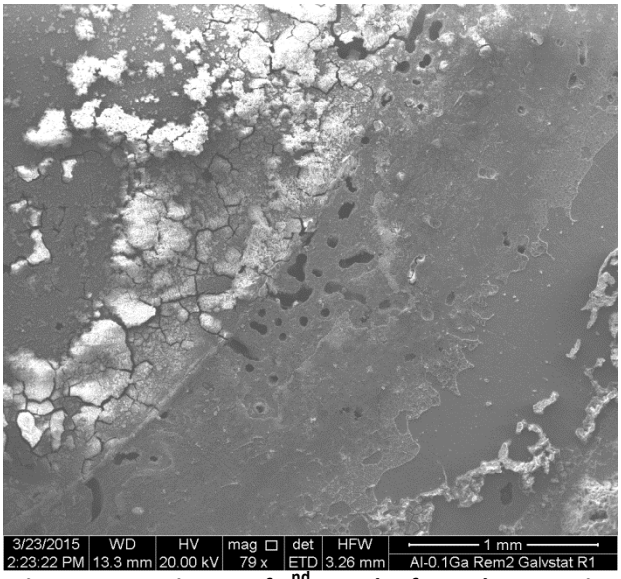

Figure 24 SEM image of 2nd remelt after galvanostatic testing, showing pits at and under O-ring interface. The pits did not appear to greatly affect the steady potential

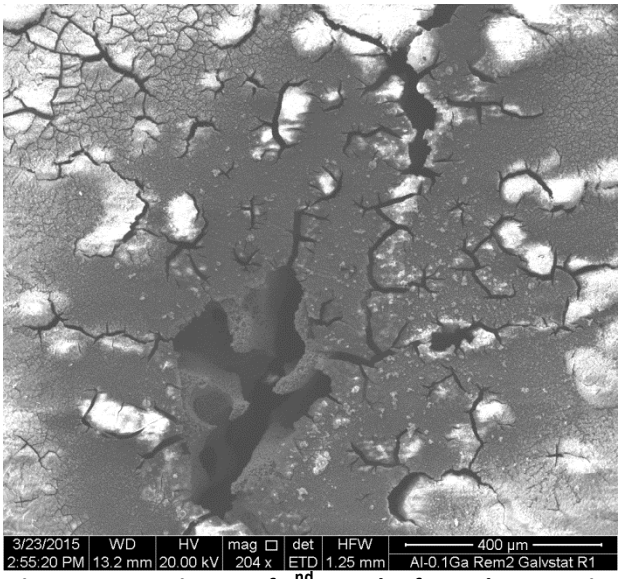

Figure 25: SEM image of 2nd remelt after galvanostatic testing, showing cracked-mud appearance, which indicates local attack underneath the oxide layer

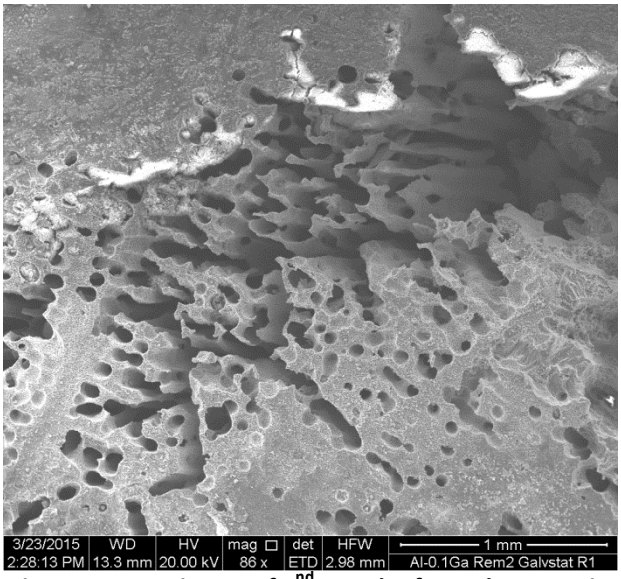

Figure 26: SEM image of 2nd remelt after galvanostatic testing, showing columns at base of sample, exhibiting different corrosion morphology than in shorter tests

3.4 Potentiodynamic

Potentiodynamic tests were conducted by scanning the potential from a low and cathodic starting potential and sweeping up to a high and anodic one. Initial runs scanned from -2000 mV to 0 mV, then further runs refined the range to -1800 mV to -600 mV. It was found that scan range did not significantly affect the results. 3 runs each were performed for the master heat and 1st remelt, while only 2 were completed for the 2nd remelt. Figure 27 shows one run of each, and each heat had a well-defined Ecorr, passivation range, and transpassive potential. The master heat and 1st remelt were very similar to each other, while the 2nd remelt had a slightly higher Ecorr.

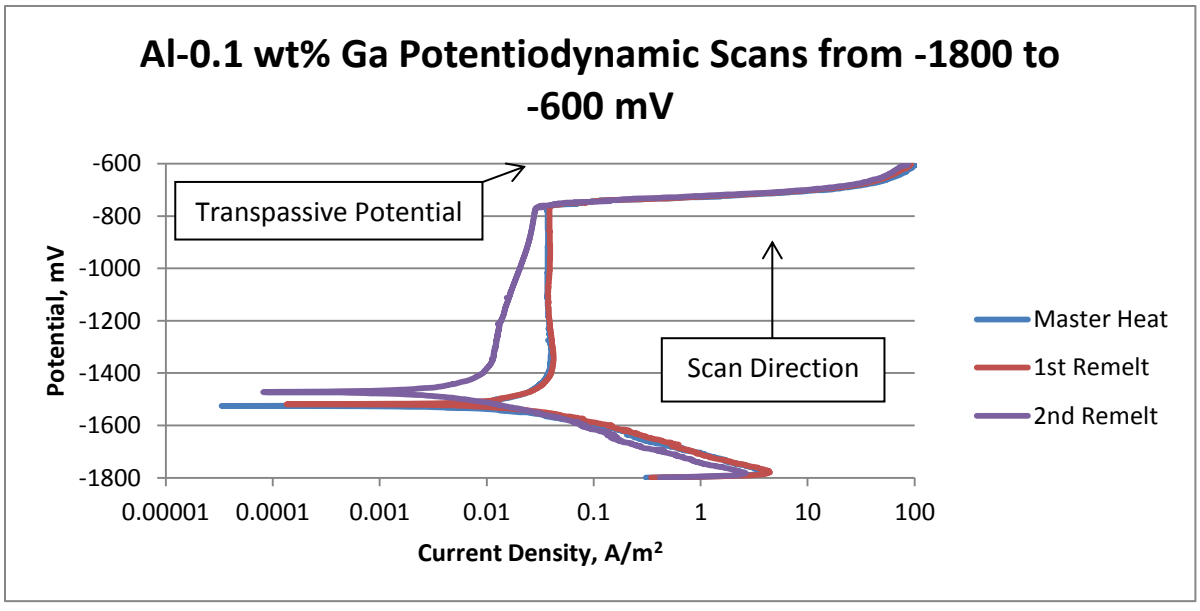

Figure 27: Al-0.1 wt% Ga Potentiodynamic scans, showing similarity of master heat and 1st remelt, with difference for 2nd remelt

The average Ecorr and transpassive potential for each heat are shown in Table 4.

Table 4: Average Ecorr and Transpassive potential

	Ecorr (mV)	Transpassive E (mV)
Master	-1540	-754
1st Remelt	-1527	-775
2nd Remelt	-1484	-756

3.5 Potentiostatic

3.5.1 Tests at -730 mV

Potentiostatic tests were run for 168 hours, at a constant potential -730 mV, which is the potential of pure Al with its passive oxide layer, as found by Pautasso et al [33]. This is also in the desired potential range for cathodically protecting steels, so it is important to ensure the activity of the Al anode at this potential [5]. Figure 28 shows the results of these tests, with the data smoothed using a 15-point moving average so as to reduce noise and make it easier to see differences in the data. As expected, all heats showed high current densities at -730 mV, because -730 mV was above the transpassive potential of every heat. The master heat quickly reached a high current density and then leveled off, slightly decreasing over time. The 1st remelt was slower to reach a peak current density and level off, and when it did so it was at a lower current density. The single run of the 2nd remelt behaved similarly to that of the master heat.

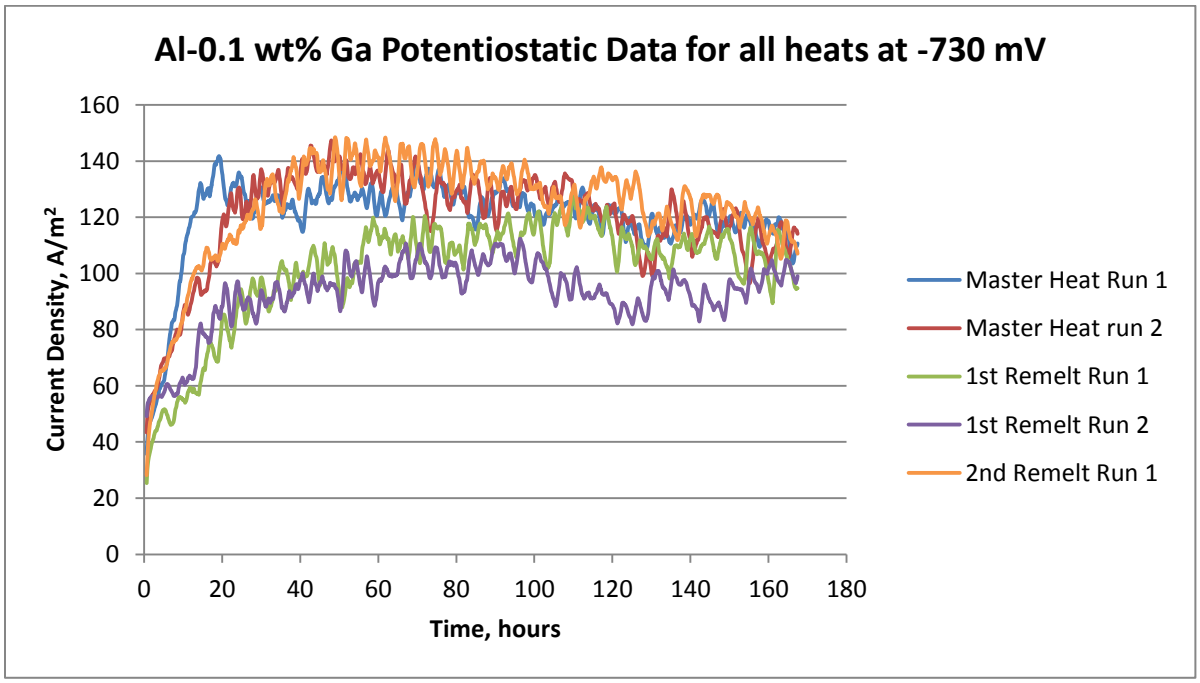

Figure 28: Al-0.1 wt% Ga Potentiostatic Data as a function of time at a constant potential of-730 mV, showing the 1st remelt with lower current densities

Table 5 summarizes the potentiostatic data, giving an average current density taken over the last 24 hours of each test.

Table 5: Average Potentiostatic Current Density over last 24 hours

Heat	Run	Current Density (A/m^2)
Master Heat	1	116.28
	2	112.76
1st Remelt	1	106.18
	2	95.85
2nd Remelt	1	118.55

3.5.2 Corroded Microstructures from Potentiostatic Tests Run at -730 mV

In general, the corroded surfaces of the samples from potentiostatic tests run at -730 mV were fairly similar to each other, with evidence of both uniform attack and some pitting, as well as the appearance of pits under the O-ring, for reasons mentioned previously. Figures 29 and 30 show the surface of the master heat, which was heavily corroded, leaving behind a rough and jagged surface. Figures 31 and 32 show the surface of the 1st remelt, which had a similar appearance to that of the master heat, but with what appeared to be grain boundaries left behind. A possible explanation for this is that the grain boundaries were more noble than the grains themselves. This observation is consistent with the discrete-particle mechanism, which involves Ga diffusion along grain boundaries. This mechanism would explain the boundaries being more noble, as they would have a higher Ga content.

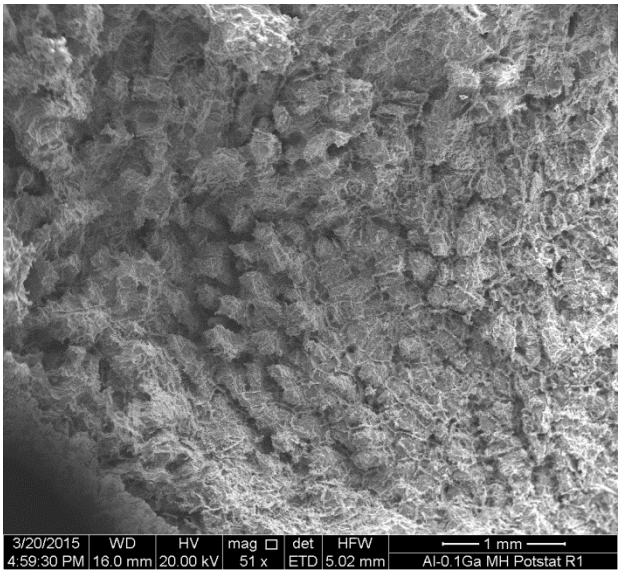

Figure 29: SEM Image of master heat after potentiostatic testing at -730 mV, showing general corroded area with rough surface

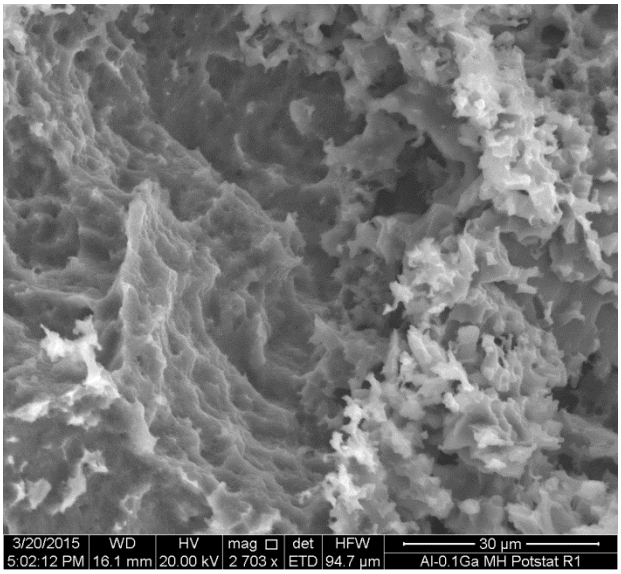

Figure 30: SEM Image of master heat after potentiostatic testing at -730 mV, showing rough and jagged corroded surface

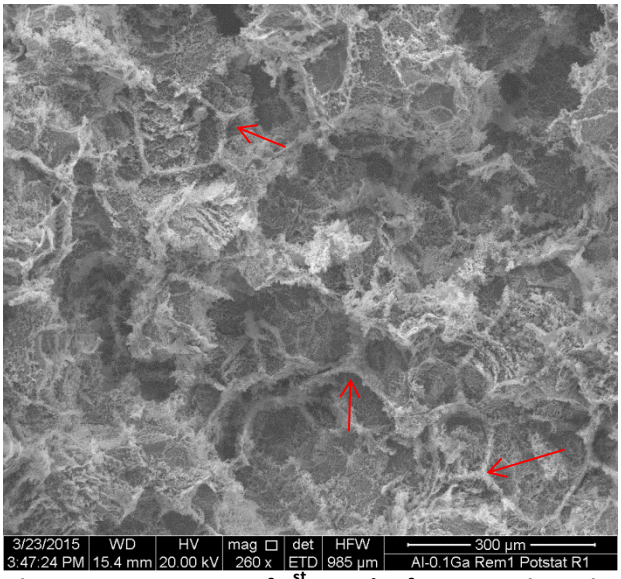

Figure 31: SEM Image of 1st remelt after potentiostatic testing at -730 mV, showing corroded area with grain boundaries left behind

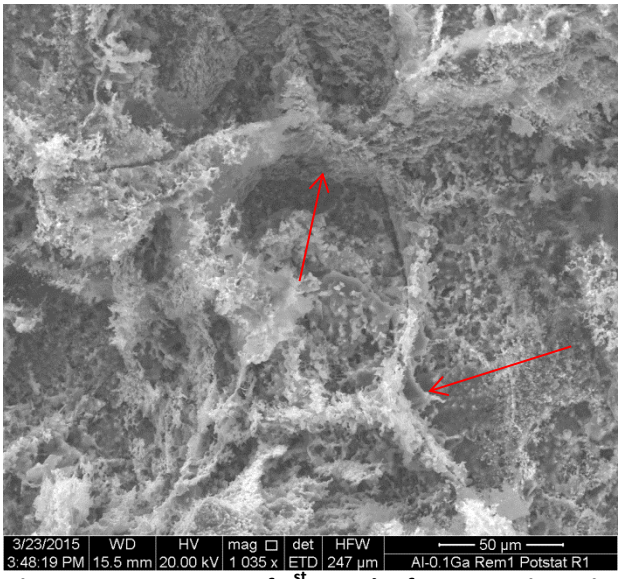

Figure 32: SEM Image of 1st remelt after potentiostatic testing at -730 mV, showing a close-up of the uncorroded grain boundaries

Figures 33 and 34 show the surface of the 2nd remelt, which has even more pronounced grain boundaries, as well as columns that were left behind, similarly to what was seen in the galvanostatic tests.

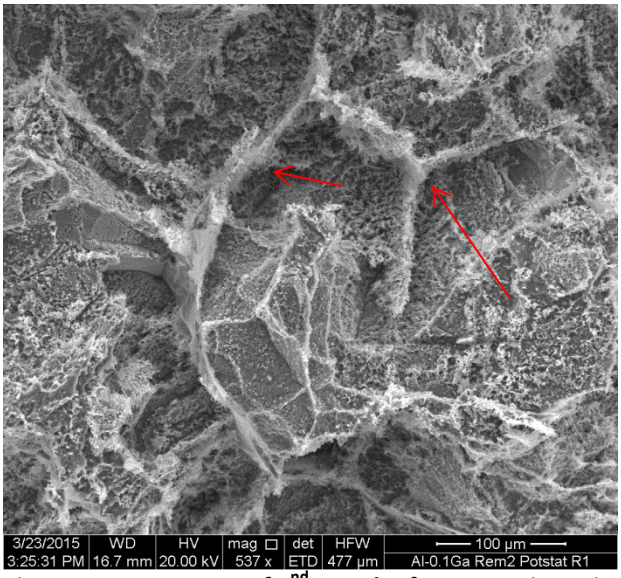

Figure 33: SEM Image of 2nd remelt after potentiostatic testing at -730 mV, showing grain boundaries left behind, even more prominently than the 1st remelt

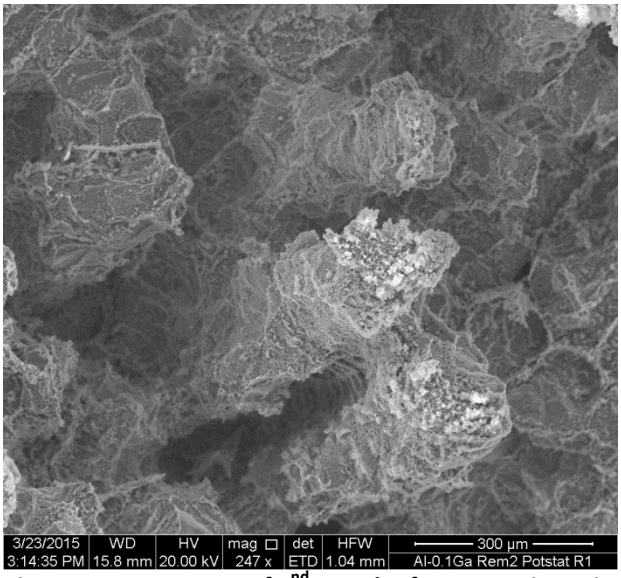

Figure 34: SEM Image of 2nd remelt after potentiostatic testing at -730 mV, showing columns left behind, similar to the galvanostatic test

3.5.3 Tests at Lower Potentials

After observing the galvanostatic behavior of the three heats, additional potentiostatic tests were conducted by holding each heat at the average potential it maintained during the steady portion of its galvanostatic test. The master heat was held at -817 mV, the 1st remelt was held at -838 mV, and the 2nd remelt was held at -846 mV. Figure 35 compares the data. The current densities are plotted on a log

scale in Figure 35. The current densities differed by three orders of magnitude between the master heat and the two remelts.

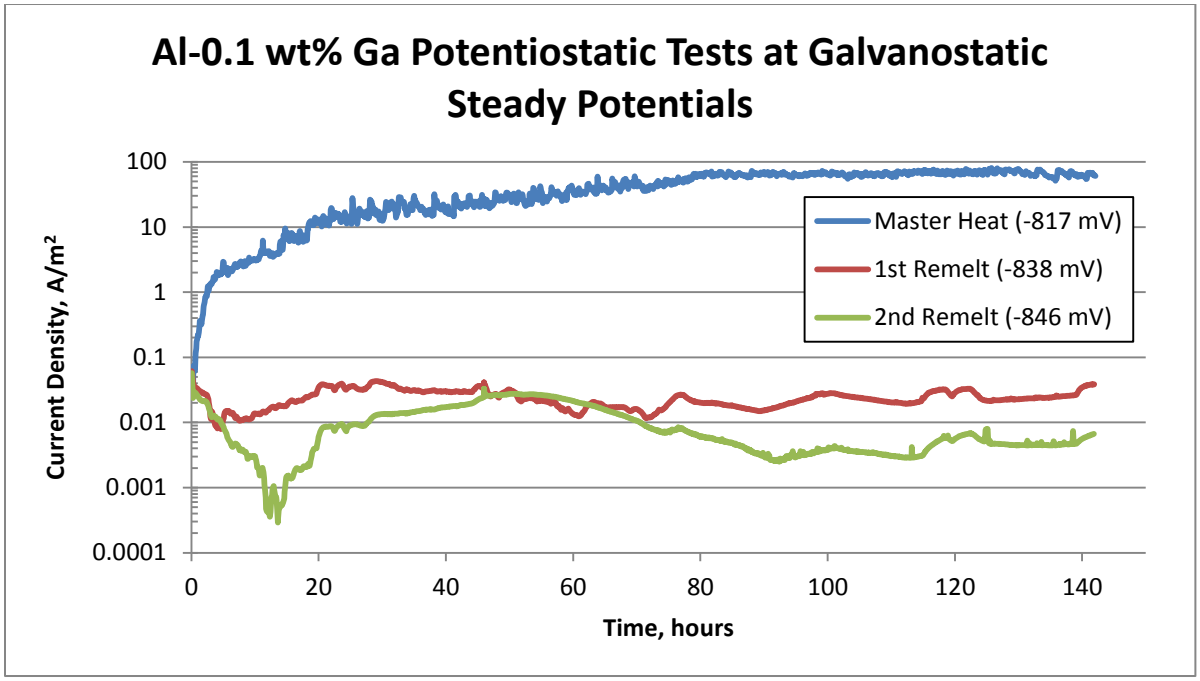

Figure 35: Current density as a function of time for the three Al-0.1 wt% Ga heats at their respective galvanostatic steady potentials

For the two remelts, the behavior seen in Figure 35 matches very well with the results of the potentiodynamic scans. Each of the two remelts was held above the transpassive potential and thus was within the passive potential region. For the master heat, the reason behind this behavior is unclear. Its potentiodynamic data predicts that the master heat should be just as passive as the other two heats at -816 mV, yet it reached current densities of nearly half those found at -730 mV, with a last-24-hour-average of 67.64 A/m^2. The average current densities from the last 24 hours of each test from Figure 35 are compared in Table 6.

Table 6: Potentiostatic current densities for heats at steady potentials

	Last 24 Hrs Average (A/m^2)
Master Heat	67.64
1st Remelt	0.027
2nd Remelt	0.0052

It is likely that the rapid erratic behavior observed in the master heat during galvanostatic testing has a similar cause to the behavior seen in Figure 35.

3.6 Galvanic Coupling

3.6.1 Electrochemical Data

Galvanic coupling tests were performed, each lasting 240 hours, to observe the heats' ability to protect the steel. Figure 36 shows the potential over time of all the heats, smoothed using a 15-point moving

average. This was done so as to reduce noise and make it easier to see differences in the data. Overall the heats had similar behavior, with the 1st remelt tending to run at slightly higher potentials than the other two heats. The 2nd remelt was in a similar range as the master heat.

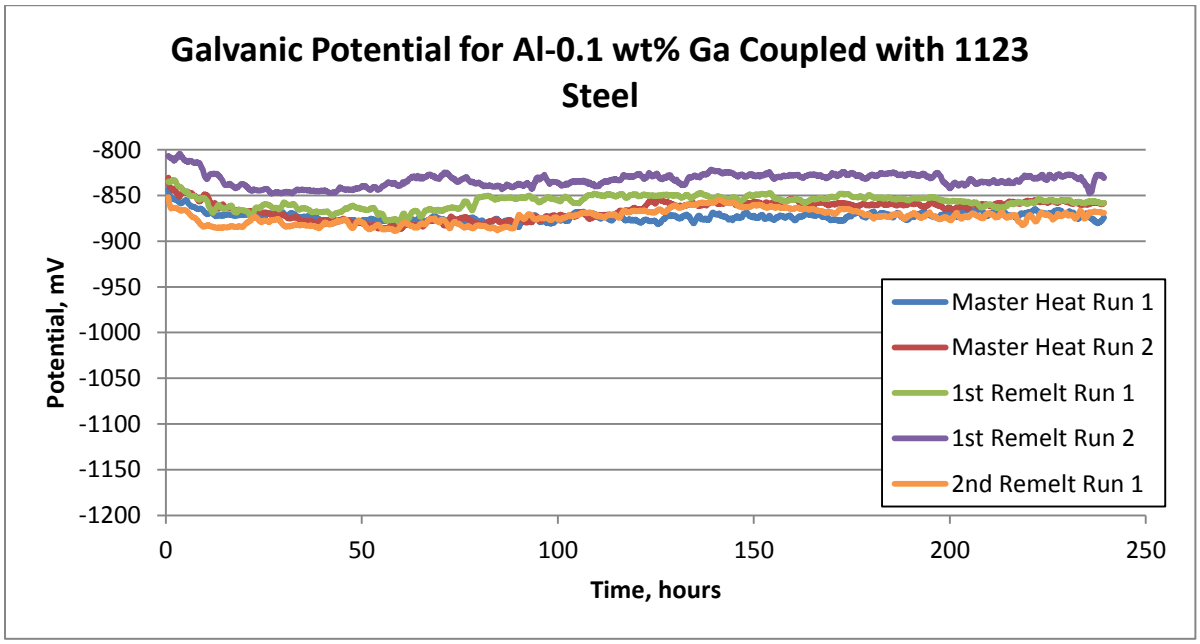

Figure 36: Galvanic Potentials for Al-0.1 wt% Ga coupled with 1123 steel as a function of time

Figure 37 shows the current densities vs time for all the heats during galvanic coupling, also smoothed using a 15-point sliding average. The currents started off fairly high but gradually leveled off over the course of a few days. All the heats had similar current densities.

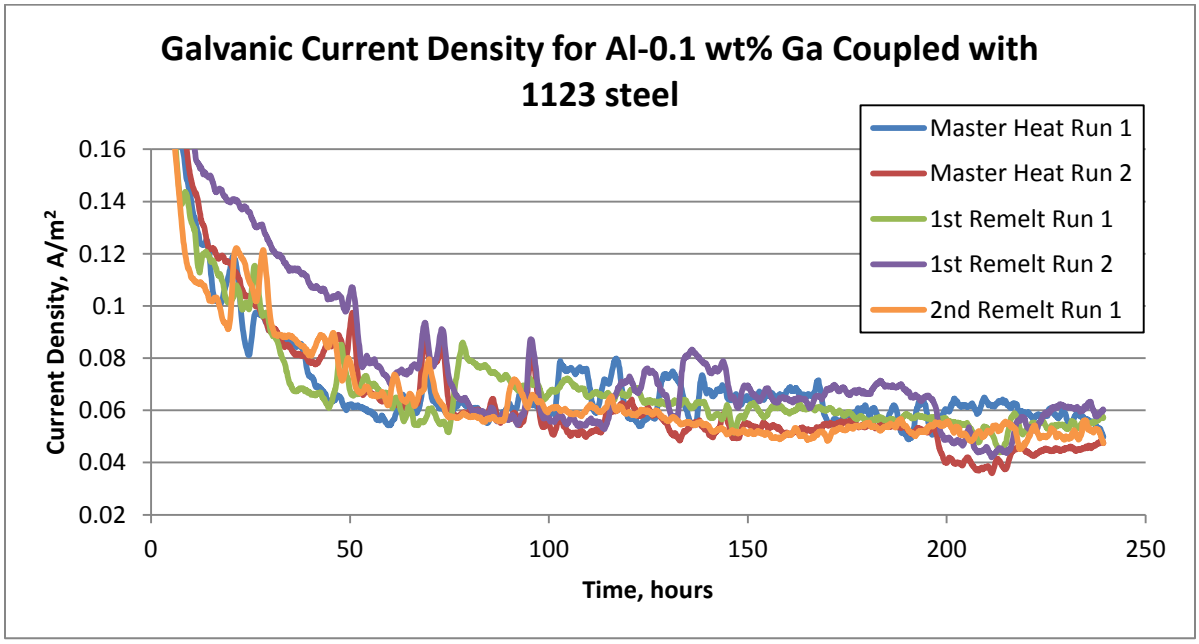

Figure 37: Galvanic current density for Al-0.1 wt% Ga coupled with 1123 steel as a function of time

Table 7 summarizes the potentials and current densities of the galvanic tests, each averaged over the last 24 hours. The galvanic current densities are slightly higher than what was observed at the potentials from Table 7 during potentiodynamic scans. This increase in current densities could be from the steel driving the corrosion of the Al, iron ions in solution affecting corrosion, or other factors.

Table 7: Galvanic potentials and current densities, each averaged over the last 24 hours of each test

Heat	Run	Potential (mV)	Current Density (A/m^2)	Current Density from Potentiodynamic Scan (A/m^2)
Master	1	-871	0.0575	0.0373
	2	-858	0.0452	0.0373
1st Remelt	1	-857	0.0548	0.0388
	2	-831	0.0583	0.0387
2nd Remelt	1	-872	0.0507	0.0257

3.6.2 Corroded Microstructures from Galvanic Coupling

All three heats had pits on their exposed surfaces as well as under the O-ring, with the master heat having more pits than either of the two remelts. Figures 38 and 39 show the exposed surface of the master heat, showing a generally smooth surface, aside from built-up deposits of seawater residue and possible corrosion products, as well as a similar cracked-mud appearance to what was seen in the galvanostatic sample. Figures 40 and 41 show the 1st remelt, with a similar smooth overall appearance, with a few pits observed.

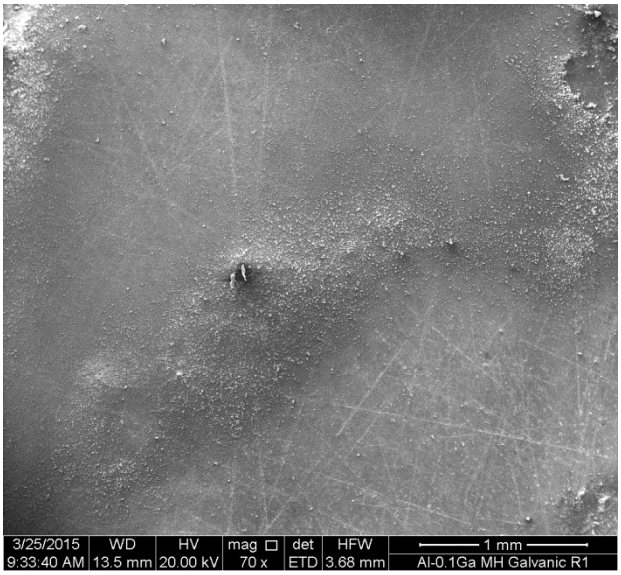

Figure 38: SEM image of master heat after galvanic coupling, showing general appearance and smooth exposed surface

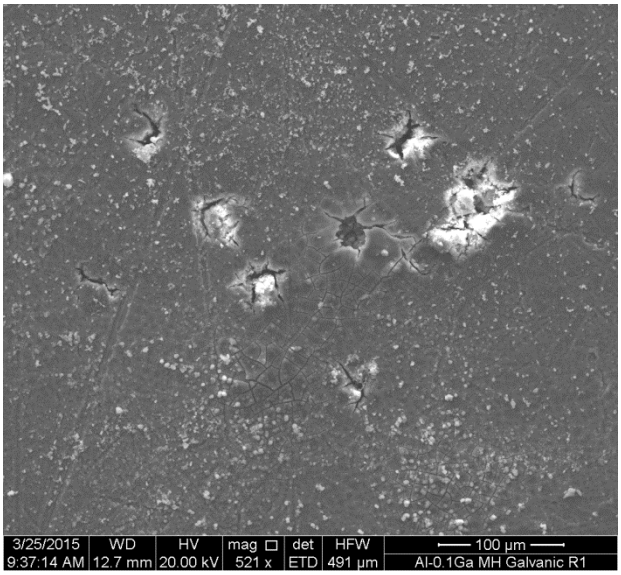

Figure 39: SEM image of master heat after galvanic coupling, showing cracked-mud pits which indicate subsurface attack

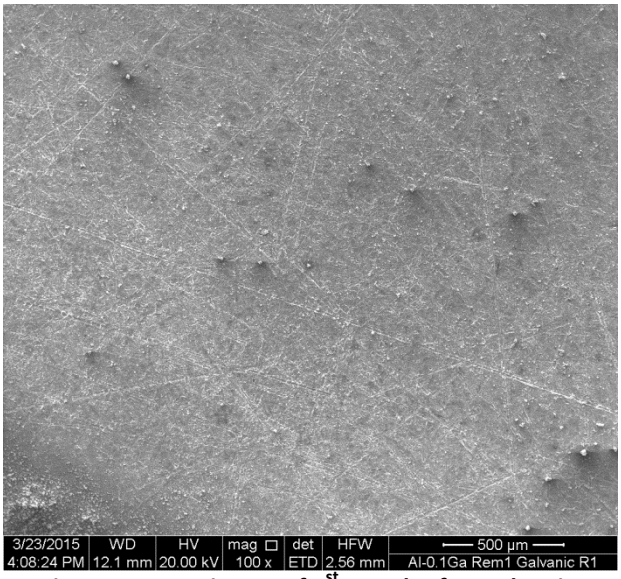

Figure 40: SEM image of 1st remelt after galvanic coupling, showing general smooth surface

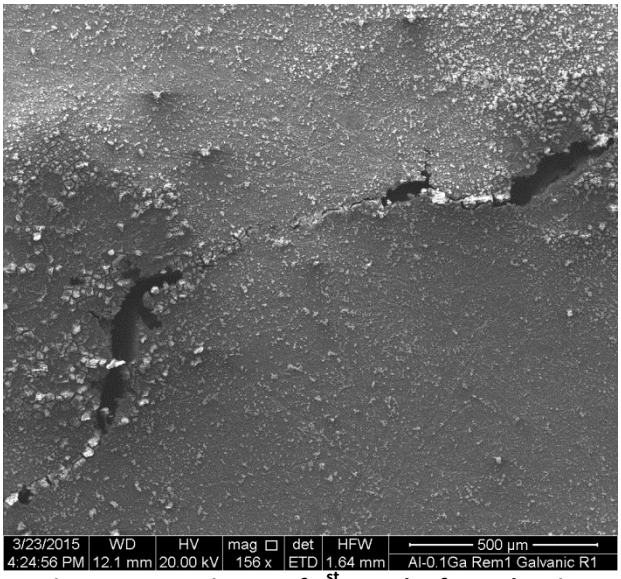

Figure 41: SEM image of 1st remelt after galvanic coupling, showing elongated pits on surface

Figures 42 and 43 show the 2nd remelt, again with a similar smooth appearance and some pits, most of which were filled with deposits.

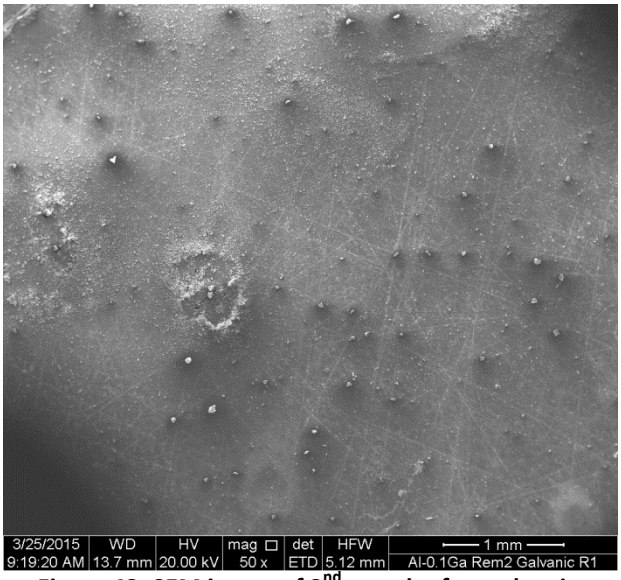

Figure 42: SEM image of 2nd remelt after galvanic coupling, showing general smooth surface

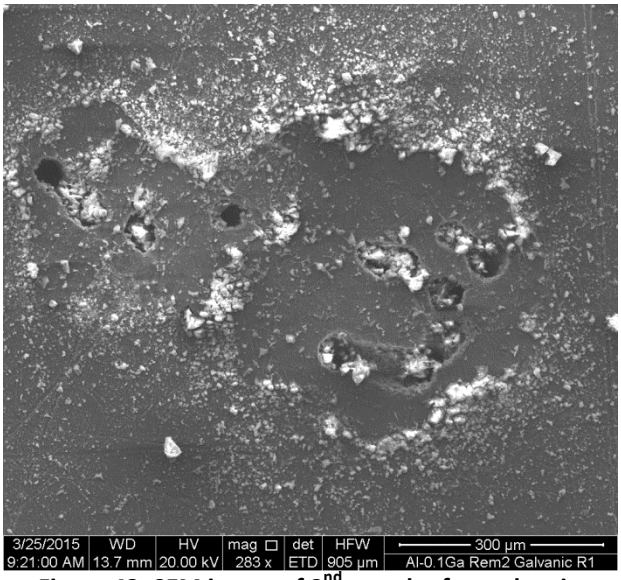

Figure 43: SEM image of 2nd remelt after galvanic coupling, showing pits filled with deposits

This localized film cracking is consistent with the discrete-particle mechanism, and it disagrees with the amalgam-layer mechanism because there is no sign of broad oxide detachment or uniform corrosion.

3.7 Effect of Heat Treatment

3.7.1 Galvanostatic Tests

A brief study was performed to obtain an overview of the effect of heat treatment on the electrochemical behavior for Al-0.1 wt% Ga. Samples taken from the July 2014 master heat were given

two heat treatments: solutionize at 538°C for one hour followed by a water quench, and artificially age at 121°C for 24 hours followed by air cooling. Overall, there was not a notable difference in behavior between either of those two heat treatments and the as-cast sample. Figure 44 shows the results of the galvanostatic test on the solution treated sample (at 9 A/m^2, the same as the July master heat).

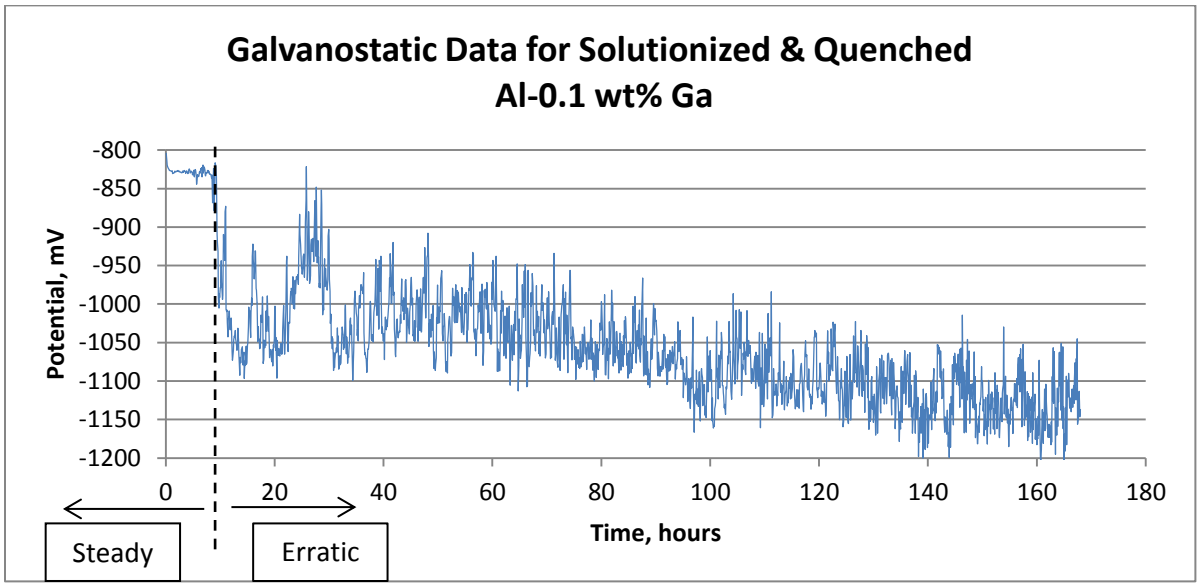

Figure 44: Al-0.1 wt% Ga galvanostatic data for solutionized and quenched sample, with similar behavior to as-cast master heats

The solutionized and quenched sample behaved similarly to the as-cast master heat from Figure 10, reaching a steady potential within an hour or so, maintaining that potential for another two to three hours, and then quickly decreasing potential, accompanied by large fluctuations. Towards the end of the test the potential settled into a range between -1050 mV and -1200 mV, similar to the as-cast sample from Figures 10.

The artificially aged sample had very similar behavior to the solutionized and quenched sample, as seen in Figure 45. It also reached a steady potential within an hour, maintained that potential for another three to four hours, and then decreased potential with fluctuations, though the fluctuations were smaller than those seen in Figures 10 and 12. The potential for the artificially aged sample eventually settled into a range between -1050 mV and -1150 mV, similar to the as-cast master heat.

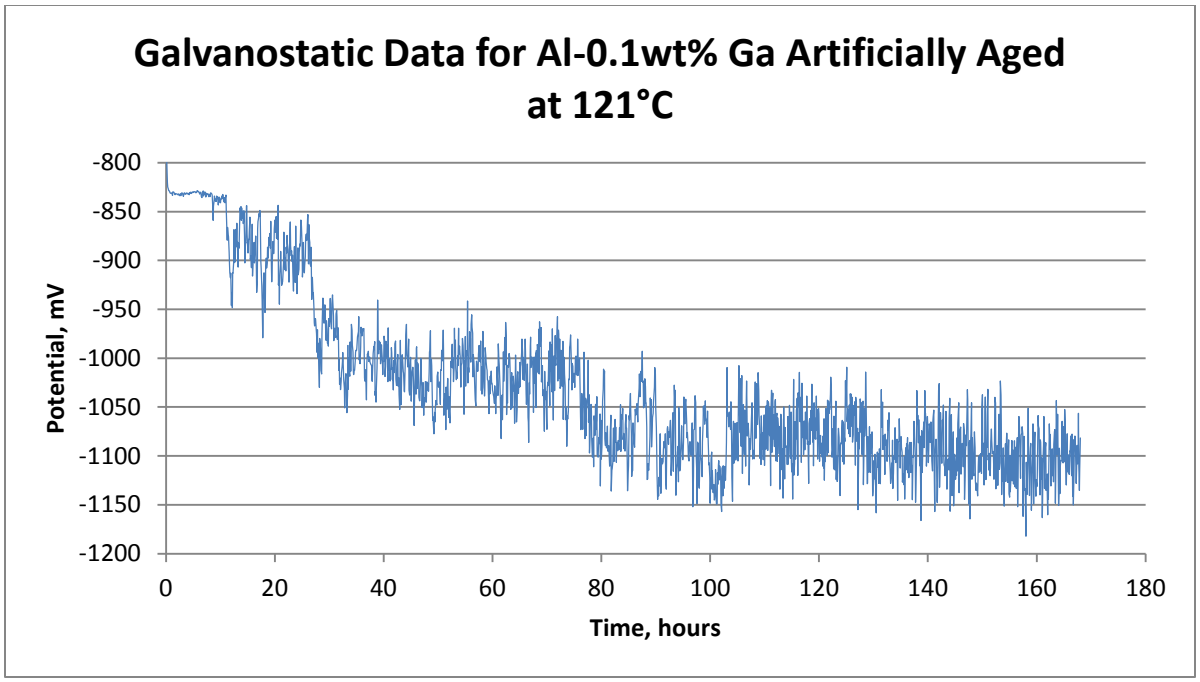

Figure 45: Al-0.1 wt% Ga galvanostatic test data for artificially aged sample, with behavior similar to as-cast and solutionized samples

As these data show, heat treating, whether by solutionizing or aging, did not have a significant effect on the galvanostatic behavior of a master heat. This is not surprising, as Ga should be entirely in solid solution at 0.1 wt%, given that its maximum solubility in aluminum is 20 wt%.

3.7.2 Potentiostatic Test

A potentiostatic test at -730 mV was performed for 168 hours on an artificially aged sample, and the data are shown in Figure 46. The current density quickly reached high values, peaking at 266 A/m^2 at 11.75 hours, then gradually declining over the remainder of the test. The average current density over the last 24 hours of the test was 163 A/m^2. This is somewhat higher than the current densities of the master heat and remelts seen earlier in this thesis, which were around 100 to 110 A/m^2. Given that only a single potentiostatic test was run on a heat treated sample, the result is inconclusive.

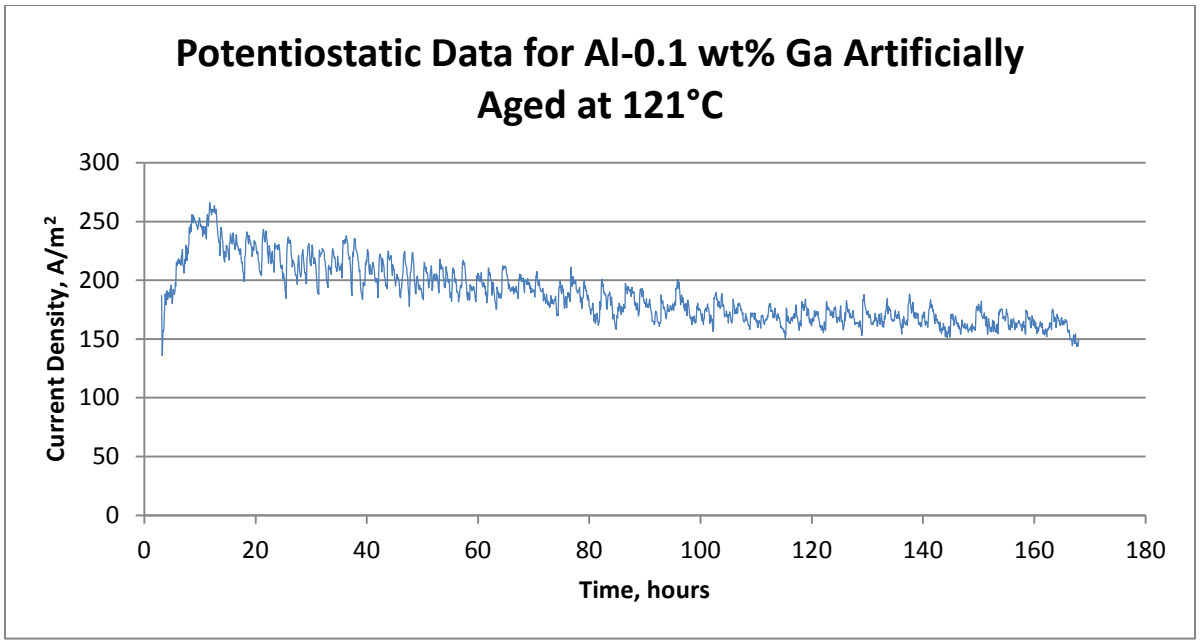

Figure 46: Potentiostatic data at -730 mV for artificially aged Al-0.1 wt% Ga sample, showing peak current density followed by gradual decline

3.8 Corrosion Rates, Current Capacities, and Anode Efficiencies

Corrosion rates were calculated from the measured weight loss of each sample tested, using equation 1:

$$Corrosion\ Rate\ \left(\frac{mg}{hr*m^2}\right) = \frac{Initial\ mass\ (mg) - Final\ mass\ (mg)}{Duration\ of\ test\ (hr)*Exposed\ Area\ (m^2)} \quad (1)$$

The theoretical current capacity of an anode is the calculated amount of energy required to oxidize a given mass of the anode. Larger current capacities are preferred because an anode of a given mass can provide more current and protection longer than an anode with a lower capacity. A sample calculation for the theoretical current capacity for pure Al is shown in equation 2.

$$Theoretical\ Capacity\ Al\ \left(\frac{A*hr}{m^2}\right) = \frac{3e^-}{1\ atom\ Al} * \frac{1.602*10^{-19}Coul}{e^-} * \frac{6.02*10^{23}atom}{mol} * \frac{1\ mol\ Al}{26.98g\ Al} * \frac{1000g}{kg} * \frac{1\ hr}{3600s} = 2978.76\ \frac{A*hr}{kg} \quad (2)$$

The theoretical current capacity for pure Ga, from equation 2, is 1152.66 A-hr/kg. Equation 3 was used to calculate the theoretical capacity for Al-0.1 wt% Ga, according to the rule of mixtures and using weight fractions:

$$Theoretical\ Capacity\ Al - 0.1Ga\ = 0.999(2978.76) + 0.001(1152.66) = 2976.94\left(\frac{A*hr}{kg}\right) \quad (3)$$

Measured current capacities were calculated by dividing the average current density for a given test run by the corrosion rate of that run. Galvanostatic tests had constant current densities, but for

potentiostatic tests the average current density was found by integration using the trapezoid rule. Anode efficiencies were calculated by dividing the measured current capacity by the theoretical current capacity. The results for the galvanostatic tests are shown in Table 8. Efficiency over 100% implies that the actual current capacity was greater than what was theoretically possible, indicating that the sample could have passivated or that there could have been something wrong with that sample's measurements. The most likely reason was that the sample had excess buildup of corrosion products and seawater residue, leading to a higher-than-actual final weight and thus a smaller corrosion rate, which in turn gave a high current capacity. Most of the as-cast runs had efficiencies around 97%, with the master heat run 1 and the 2nd remelt run 2 being exceptions. The heat treated samples had much lower efficiencies, around 40%. It is unclear whether this difference in efficiency is due to the effect of heat treatment, current density, or pieces falling off of the sample. The mass losses seen in the galvanostatic tests were fairly low, around 30 mg, so the results are also more prone to measurement error.

Table 8: Galvanostatic Current Capacities and Anode Efficiencies

Heat	Run	Current Density (A/m^2)	Corrosion Rate ($mg/hr/m^2$)	Current Capacity (A*hr/kg)	Efficiency
Master	1	6.2	1785.7	3472.0	116.6%
	2	6.2	2142.9	2893.3	97.2%
1st Remelt	1	6.2	2142.9	2893.3	97.2%
	2	6.2	2142.9	2893.3	97.2%
2nd Remelt	1	6.2	2217.3	2796.2	93.9%
	2	6.2	2154.6	2877.5	96.7%
	4	6.2	2678.6	2314.7	77.8%
Aged	1	9	7901.8	1139.0	38.3%
Solution	1	9	7366.1	1221.8	41.0%

The results from the potentiostatic tests are shown in Table 9. As seen in Figure 28, all three heats had high current densities and severe corrosion, which is reflected in the high corrosion rates in Table 9. These higher corrosion rates led to less sensitivity to measurement error. The efficiencies of all the as-cast samples were in the 95% to 96% range, with the artificially aged sample having a slightly lower efficiency around 93%.

Table 9: Potentiostatic Current Capacities and Anode Efficiencies

Heat	Run	Integrated Average Current Density (A/m^2)	Corrosion Rate ($mg/hr/m^2$)	Current Capacity (A*hr/kg)	Efficiency
Master	1	120.1	42381.0	2834.6	95.2%
	2	119.8	42142.9	2843.7	95.5%
1st Remelt	1	101.4	35535.7	2852.2	95.8%
	2	92.9	32619.1	2846.4	95.6%
2nd Remelt	1	123.5	43214.3	2857.0	96.0%
Aged	1	187.7	67916.7	2763.7	92.8%

All of the as-cast samples' efficiencies found in this study compare very favorably to those of other alloys found in an earlier study, such as Al-2 wt% Bi (74.5%), Al-0.49 wt% Zn (80.7%), Al-0.01 wt% In (87.7%), and many others [35].

3.9 X-Ray Photoelectron Spectroscopy (XPS)

3.9.1 Uncorroded samples

For each heat, one sample that had not undergone corrosion testing was examined using XPS. An initial survey of the samples before sputtering did not show any Ga signal, but after a 1 min sputter with 3keV Ar^+, a faint but distinct Ga peak appeared on all three samples. This signal began to disappear below the detection limits of the machine with further sputtering. The Ga contents in atom % found are shown in Figure 47. The 1st remelt had a lower measured Ga content than the Master Heat and 2nd remelt, but all three Ga contents were much higher than the nominal bulk composition of 0.04 at% (0.1 wt%).

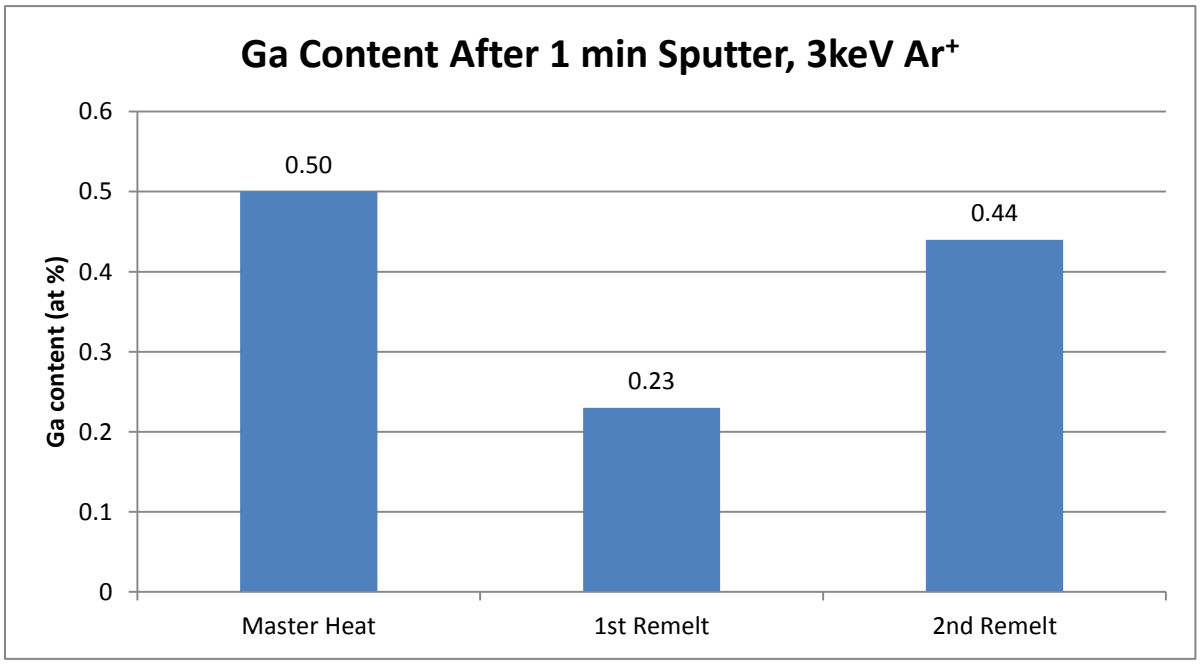

Figure 47: Ga content of uncorroded samples after 1 minute sputter, showing elevated levels of Ga just below sample surface, indicating that Ga is present in Al oxide layer

3.9.2 Corroded Samples

Two samples each from the master heat and the 1st remelt were exposed to galvanostatic conditions in seawater at 6.2 A/m^2. For the first remelt, one sample was run until the potential began to quickly fall (25 hours) and was labeled as erratic. The other sample test was stopped while the potential still maintained a steady value (24 hours) and labeled as steady. For the master heat, one sample was run for about 1.5 hours (short) and the other for 3.75 hours (long). Both maintained a steady potential for their entire durations. Depth profiles of Ga, Al, and O were taken on each sample using 1 minute increments of sputtering with 3keV Ar^+. Figure 48 shows the Ga profile for each sample. The Ga contents were low and close to the detection limits of the instrument, so the data contained a large amount of noise. Few clear trends could be established due to the noise, but both the master heat samples had

consistently higher Ga contents than the 1st remelt samples ($p<0.006$). There were no significant differences between the two master heat samples ($p>0.15$), showing that the duration of the test had little effect on the Ga profile, so long as the potential remained steady. This shows that there are elevated levels of Ga within the oxide, but that the onset of erratic potentials does not drastically change the Ga content; thus it does not support the amalgam-layer mechanism.

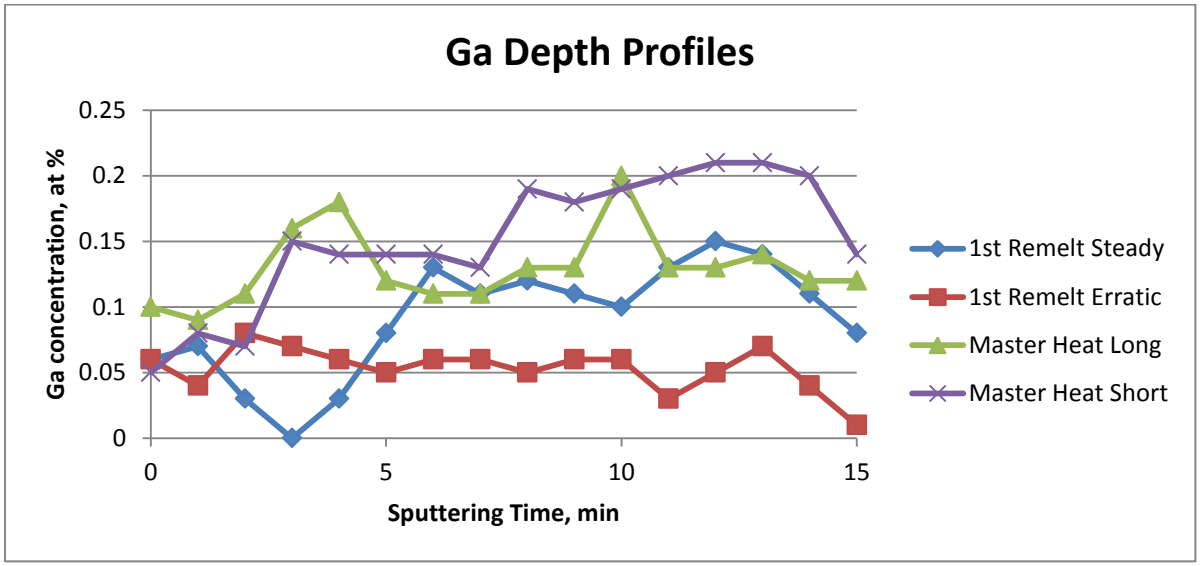

Figure 48: Ga depth profiles, showing master heat with higher Ga contents than 1st remelt

Figure 49 shows the O depth profiles for all four samples. The 1st remelt had higher O content than the master heat throughout, and based on the plateau observed in the 1st remelt, the oxide layer was indeed thicker than that of the master heat. The active 1st remelt sample also had much higher O content than the steady sample and thus a thicker oxide layer. This does not support the amalgam-layer mechanism, which would result in widespread thinning and detachment of the oxide layer.

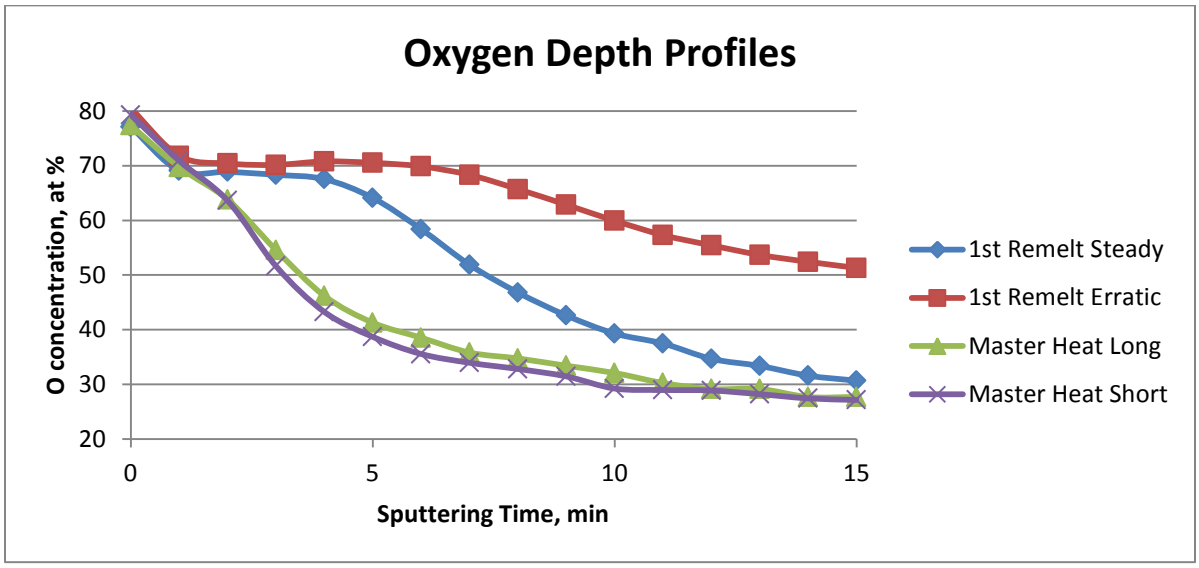

Figure 49: Oxygen depth profiles, showing higher O content and thicker oxide layers in 1st remelt than in master heat

4. Conclusions

The effect of remelting an Al-0.1 wt% Ga alloy was characterized using open circuit, galvanostatic, potentiodynamic, potentiostatic, and galvanic corrosion tests. Corroded microstructures were observed using a SEM. The effect of heat treating on electrochemical behavior of a master heat was quickly examined. Corrosion rates, current capacities, and anode efficiencies were calculated. Surface compositions and depth profiles were measured using XPS.

The inconsistent behavior of Al- 0.1 wt% Ga master heats was confirmed, and remelting was shown to reduce the variability. Remelting increased the nobility of grain boundaries. All anodes served to protect the steel in galvanic coupling, as they all had active current densities and operated within or near the desired potential range of -750 to -850 mV. All three heats had good anode efficiencies, generally greater than 95%. Ga was found at elevated levels below the ground surface of uncorroded samples, with varying levels of Ga through the depth of corroded samples.

Overall, the data did not support the amalgam-layer mechanism but were consistent with the discrete-particle mechanism. Further work is needed in order to further elucidate this mechanism and confirm actual mechanism.

4.1 Potential Sources of Error

This research had some potential sources of error. The typical data acquisition rates used in this work were typically one data point taken every five minutes, which was deemed a good compromise, given that the tests were being run for 168 or 240 hours. The surface finish was 600 grit, which is a particle size of about 10 microns; that level of roughness could certainly contribute to variation across tests, and especially lead to additional noise and variation in XPS analysis. 600 grit was within the range of surface finishes found in the literature, which ranged from 400 grit [15] to 0.3 µm [23]. In all tests, the seawater electrolyte was not stirred, pumped, flushed, or replaced for the duration of each test. This allowed corrosion products and salt deposits to build up inside the test cells, which can affect further corrosion. This buildup was especially evident in the potentiostatic tests at -730 mV, where the electrolyte became nearly opaque by the end of the test. As mentioned before, crevice corrosion was observed on all the samples viewed on the SEM; crevice effects can cause premature and accelerated corrosion and thus lead to errors in measured potential, current density, and mass loss. Additionally, not all of the corrosion products and residue was cleaned from the tested samples, especially from inside occluded pits; this can skew corrosion rates to appear smaller than they actually were, as the final masses of the samples would be measured higher than actual.

4.2 Future Work

There are many avenues for further research on the behavior of Al-0.1 wt% Ga anodes in seawater:

- A full investigation of the effects of heat treatment on microstructure and corrosion behavior
- The effects of surface finish on corrosion
- The effects of pH
- The effects of solution flow rate, both through the cell and across the anode
- The effects of dissolved oxygen in the seawater

The flat cell experimental setup could be modified to eliminate crevice corrosion and pitting under the O-ring. Longer tests should be run in order to truly observe the anodes' behavior under the long time periods they will face in real-world use. Secondary ion mass spectrometry (SIMS) and transmission electron microscopy (TEM) could be used to obtain higher-resolution data about the depth profile, concentration, and location of the Ga in the alloy. Higher data acquisition rates should be used when activation is anticipated in order to catch the exact moment when it occurs. This would also give a more accurate picture of the fluctuation of potentials in the galvanostatic tests.

Given the discrete-particle activation mechanism, the ideal behavior for an Al-0.1 wt% Ga anode would consist of the Ga particles being distributed uniformly across the surface of the anode in order to maximize the homogeneity of the localized corrosion.

To further elucidate the mechanism of activation of Al by Ga, some critical experiments should be performed. These include TEM analyses of the anodes taken at different time intervals of corrosion, in order to observe the formation and distribution of the Ga particles. SIMS depth profiles of anodes taken at these time intervals would also show how the oxide layer changes with time, how it thins near Ga particles but possibly thickens far away from them, as shown in the XPS profile of the active 1st remelt sample. Additional galvanostatic testing should be performed in order to obtain a greater sample size for each remelt, as well as varying the current densities to better match those seen in the galvanic coupling tests. Further galvanic coupling tests, varying the area ratios of the cathode to the anode, would give results closer to true service conditions, as the current flat cell setup uses an area ratio of 1:1. Corrosion tests should be run for longer times as well, in order to better mimic true service lives.

References

[1] H. Davy, "On the corrosion of copper sheeting by sea water, and on methods of preventing this effect; and on their application to ships of war and other ships," *Philosophical Transactions of the Royal Society of London,* vol. 114, pp. 151-158, 1824.

[2] P. Roberge. (2015). *History of Cathodic Protection*. Available: http://www.corrosion-doctors.org/Corrosion-History/CP-History.htm

[3] P. Roberge. (2015). *Galvanic Series*. Available: http://www.corrosion-doctors.org/Definitions/galvanic-series.htm

[4] A. R. Despić, D. M. Dražić, M. M. Purenović, and N. Ciković, "Electrochemical properties of aluminium alloys containing indium, gallium and thallium," *Journal of Applied Electrochemistry,* vol. 6, pp. 527-542, 1976/11/01 1976.

[5] H. Le Guyader, "Consumable anode for cathodic protection, made of aluminum-based alloy," ed: Google Patents, 1996.

[6] J. Reding and J. Newport, "The influence of alloying elements on aluminum anodes in sea water," *Mater Protect,* vol. 5, pp. 15-18, 1966.

[7] MIL-DTL-24779C(SH) 2013, "Detail Specification, Anodes, Sacrificial, Aluminum Alloy" (Washington, DC: Naval Sea Systems Command).

[8] N. Idusuyi and O. Oluwole, "Aluminium Anode Activation Research–A Review," *International Journal of Science and Technology,* vol. 2, pp. 561-566, 2012.

[9] ACS. *Placeholder for ACS Citation about Aluminum*. Available: http://www.acs.org/content/acs/en/education/whatischemistry/landmarks/aluminumprocess.html

[10] Q. Li and N. J. Bjerrum, "Aluminum as anode for energy storage and conversion: a review," *Journal of Power Sources,* vol. 110, pp. 1-10, 2002.

[11] J. Staley, "Aluminum Anode" U.S. Patent 2 913 384, Nov. 17 1959

[12] T. Sakano, K. Toda, and M. Hanada, "Tests on the effects of indium for high performance aluminum anodes," *Mater Protect,* vol. 5, pp. 45-50, 1966.

[13] J. L. Murray, "The Al−Ga (Aluminum-Gallium) system," *Bulletin of Alloy Phase Diagrams,* vol. 4, pp. 183-190, 1983/09/01 1983.

[14] M. Reboul, P. Gimenez, and J. Rameau, "A proposed activation mechanism for Al anodes," *Corrosion,* vol. 40, pp. 366-371, 1984.

[15] C. Tuck, J. Hunter, and G. Scamans, "The Electrochemical Behavior of Al-Ga Alloys in Alkaline and Neutral Electrolytes," *Journal of the Electrochemical Society,* vol. 134, pp. 2970-2981, 1987.

[16] C. B. Breslin and W. M. Carroll, "The electrochemical behaviour of aluminium activated by gallium in aqueous electrolytes," *Corrosion Science,* vol. 33, pp. 1735-1746, 1992.

[17] N. Murer and R. G. Buchheit, "Stochastic modeling of pitting corrosion in aluminum alloys," *Corrosion Science,* vol. 69, pp. 139-148, 2013.

[18] W. M. Carroll and C. B. Breslin, "Activation of aluminium in halide solutions containing 'activator ions'," *Corrosion Science,* vol. 33, pp. 1161-1177, 1992.

[19] M. Textor and M. Amstutz, "Surface analysis of thin films and interfaces in commercial aluminium products," *Analytica Chimica Acta,* vol. 297, pp. 15-26, 1994.

[20] N. Margadant, P. Skeldon, M. Textor, G. E. Thompson, J. Wan, H. Habazaki, K. Shimizu, N. D. Spencer, and G. C. Wood, "Gallium enrichment and film detachment during anodizing of an Al–Ga alloy," *Corrosion Science,* vol. 42, pp. 405-419, 2000.

[21] E. Aragon, L. Cazenave-Vergez, E. Lanza, A. Giroud, and A. Sebaoun, "Influence of alloying elements on electrochemical behaviour of ternary Al-Zn-Ga alloys for sacrificial anodes," *British Corrosion Journal,* vol. 32, pp. 263-268, 1997.

[22] Z. Ashitaka, P. Skeldon, G. E. Thompson, K. Shimizu, and H. Habazaki, "Enrichment behaviour of gallium in heat and surface treatments of Al–Ga foils," *Corrosion Science,* vol. 44, pp. 2725-2735, 2002.
[23] D. O. Flamini, S. B. Saidman, and J. B. Bessone, "Aluminium activation produced by gallium," *Corrosion Science,* vol. 48, pp. 1413-1425, 2006.
[24] D. O. Flamini, S. B. Saidman, and J. B. Bessone, "Electrodeposition of gallium and zinc onto aluminium. Influence of the electrodeposited metals on the activation process," *Thin Solid Films,* vol. 515, pp. 7880-7885, 2007.
[25] D. O. Flamini, L. Cunci, and S. B. Saidman, "Electrochemical characterisation of gallium–aluminium amalgams," *Materials Chemistry and Physics,* vol. 108, pp. 33-38, 2008.
[26] E. Senel and K. Nisancioglu, "Role of dealloying on the electrochemical behaviour of aluminium alloyed with trace amounts of gallium," *Corrosion Science,* vol. 85, pp. 436-444, 2014.
[27] E. Senel and K. Nisancioglu, "Anodic activation of aluminium containing small amounts of gallium and tin," *Corrosion Science,* vol. 88, pp. 280-290, Nov 2014.
[28] A. Druschitz, M. Maxfield, W. Monzel, and K. Tontodonato, "A Novel Approach for the Development of Low-Voltage, Aluminum, Sacrificial Anodes," in *Corrosion 2015*, Dallas, TX, 2015.
[29] ASTM Standard D1141-98(2013), "Standard Practice for the Preparation of Substitute Ocean Water," ASTM International, West Conshohocken, PA 2013
[30] ASTM Standard G1-03(11), "Standard Practice for Preparing, Cleaning, and Evaluating Corrosion Test Specimens," ASTM International, West Conshohocken, PA 2011."
[31] ASTM Standard G5-14, "Standard Reference Test Method for Making Potentiodynamic Anodic Polarization Measurement," ASTM International, West Conshohocken, PA 2014."
[32] ASTM Standard G69-12, "Standard Practice for Measurement of Corrosion Potentials of Aluminum Alloys," ASTM International, West Conshohocken, PA 2012."
[33] J. Pautasso, H. Le Guyader, and V. Debout, "Low Voltage Cathodic Protection for High Strength Steels: Part 1–Definition of a New Aluminum Galvanic Anode," ed: Paper, 1998.
[34] "Impressed Current Laboratory Testing of Aluminum Alloy Anodes" (Houston, TX: NACE)
[35] W. Monzel, "Investigation of New, Low-Voltage, Aluminum, Sacrificial Anode Chemistries," Masters Thesis, Materials Science and Engineering Virginia Tech, 2014.

Appendices

The following appendices contain data that was collected but not shown in the thesis body, as well as some raw data.

Appendix A: Galvanostatic Data

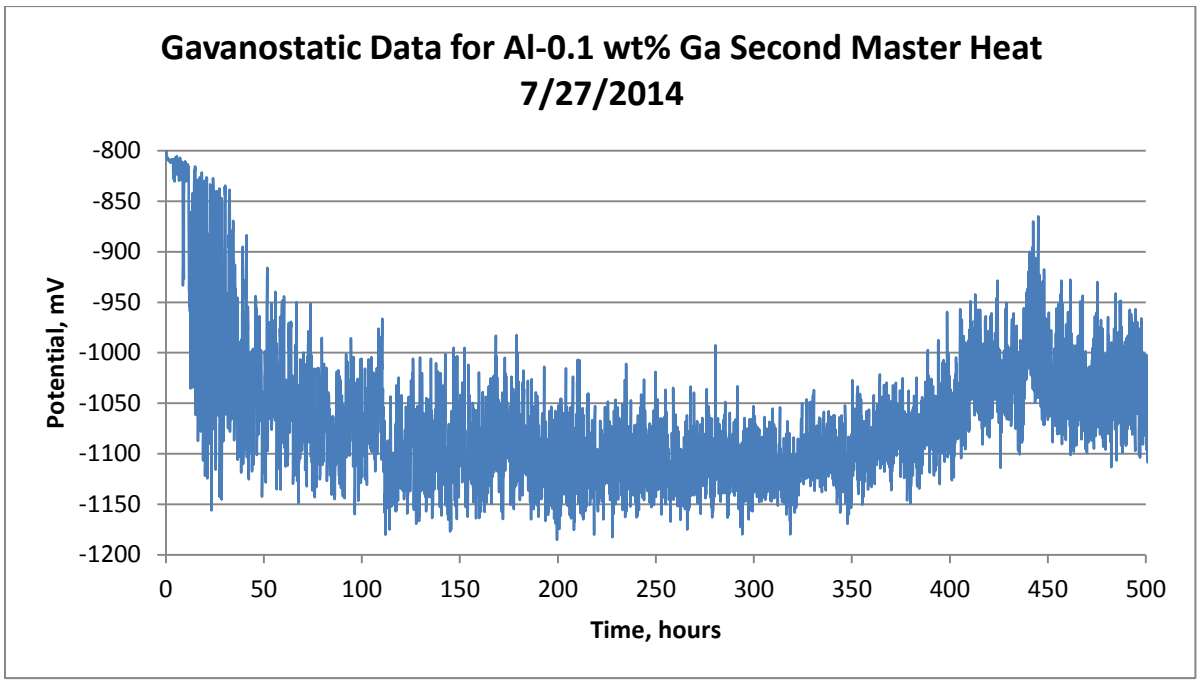

Figure 50: Galvanostatic data for Al-0.1 wt% Ga second master heat from July 2014 for 500 hours

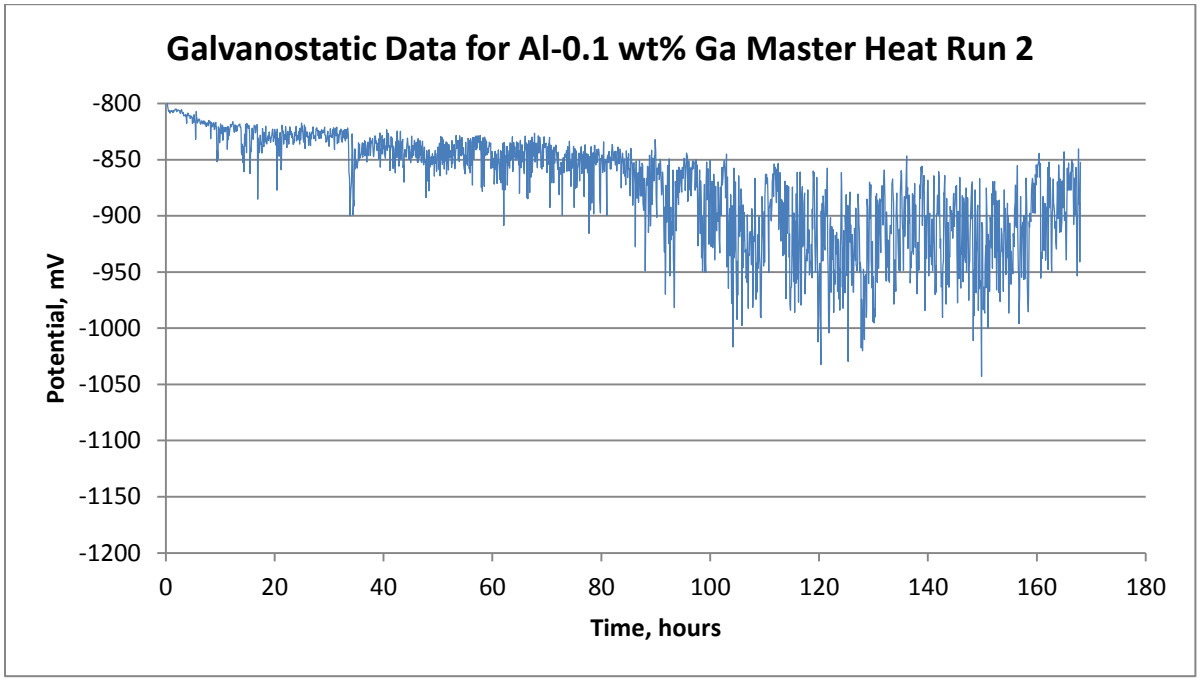

Figure 51: Galvanostatic data for Al-0.1 wt% Ga master meat run 2, similar to run 1

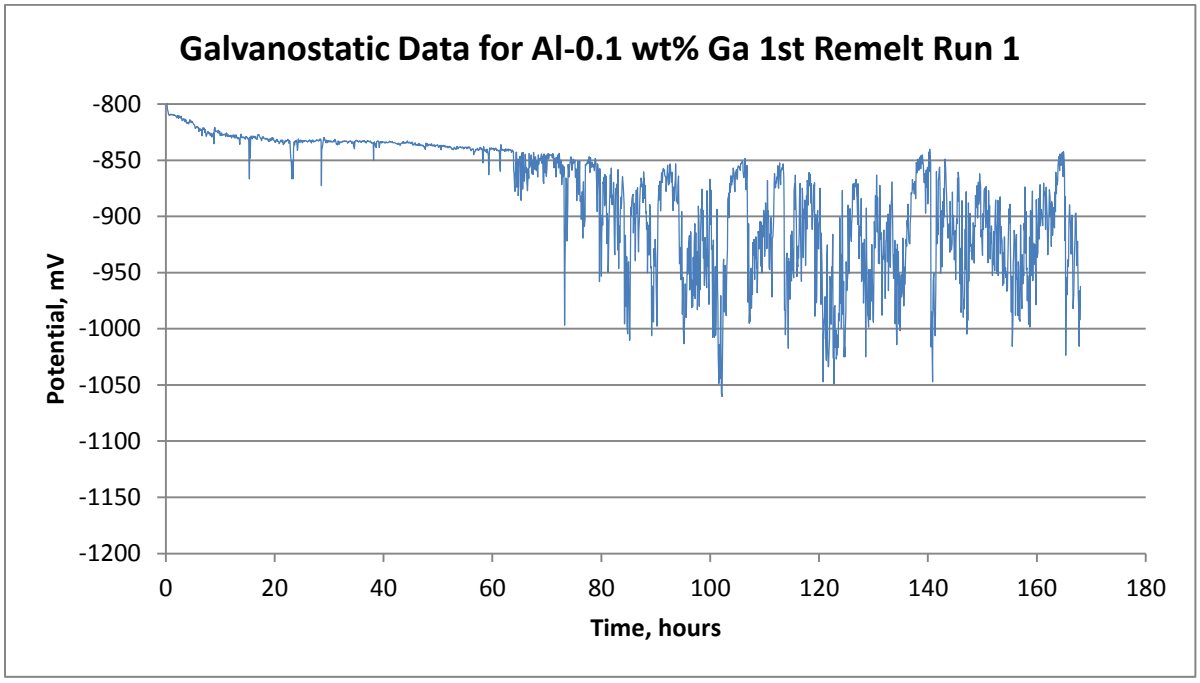

Figure 52: Galvanostatic data for Al-0.1 wt% Ga 1st Remelt run 1, similar to run 2

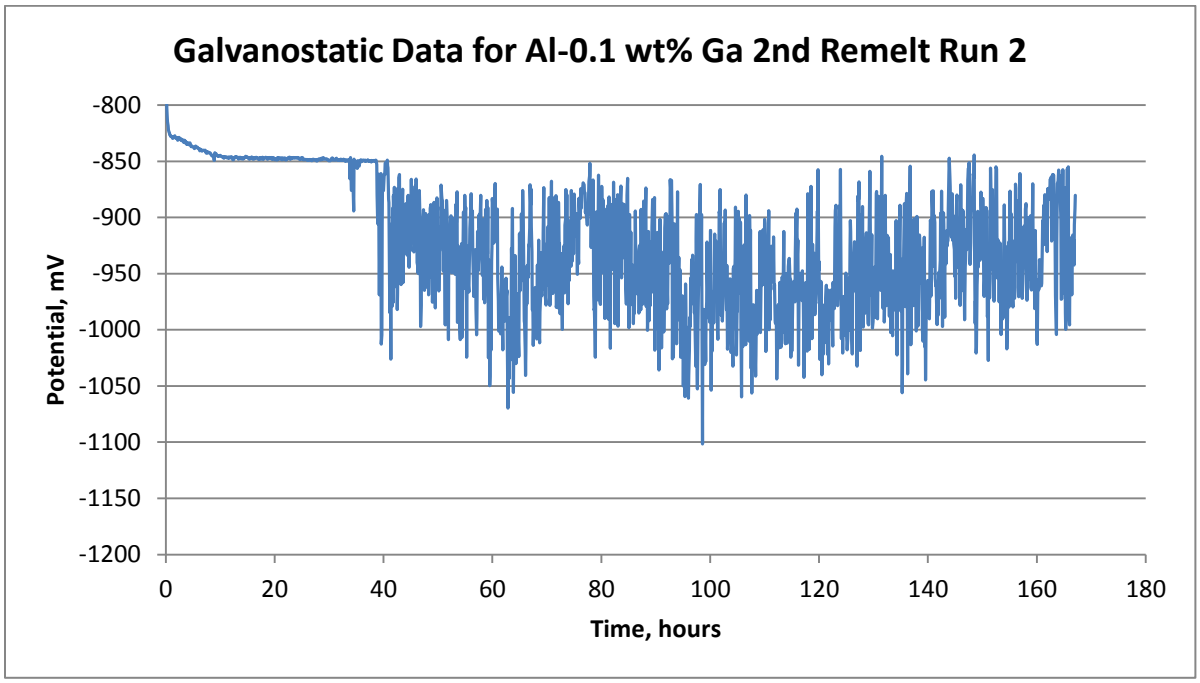

Figure 53: Galvanostatic data for Al-0.1 wt% Ga 2nd remelt Run 2, remaining steady for about 40 hours

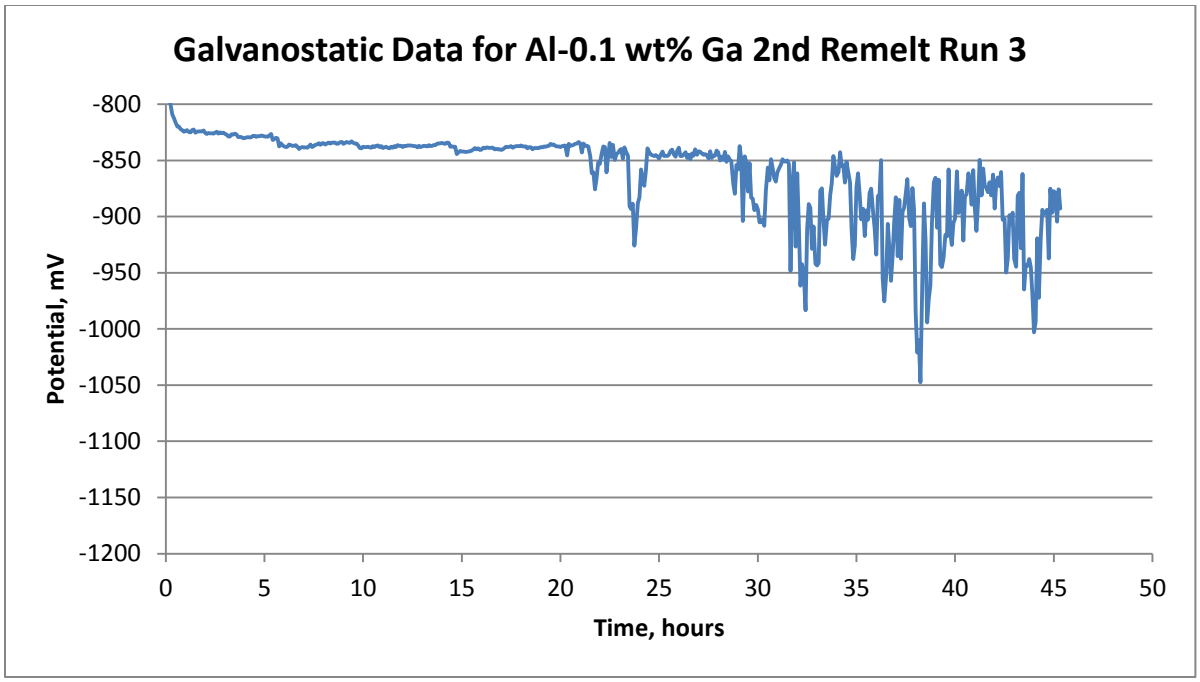

Figure 54: Galvanostatic data for Al-0.1 wt% Ga 2nd Remelt Run 3, remaining steady for 20-30 hours

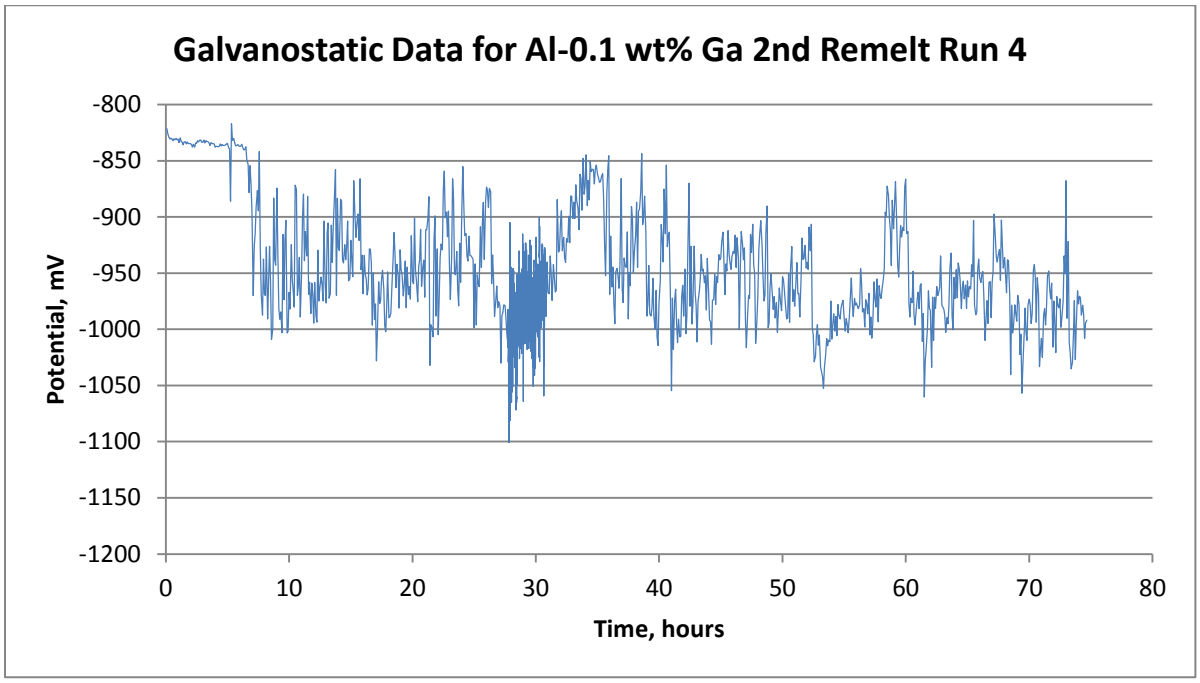

Figure 55: Galvanostatic Data for Al-0.1 wt% Ga 2nd Remelt Run 4, remaining steady for about 7 hours

Appendix B: Potentiodynamic Data

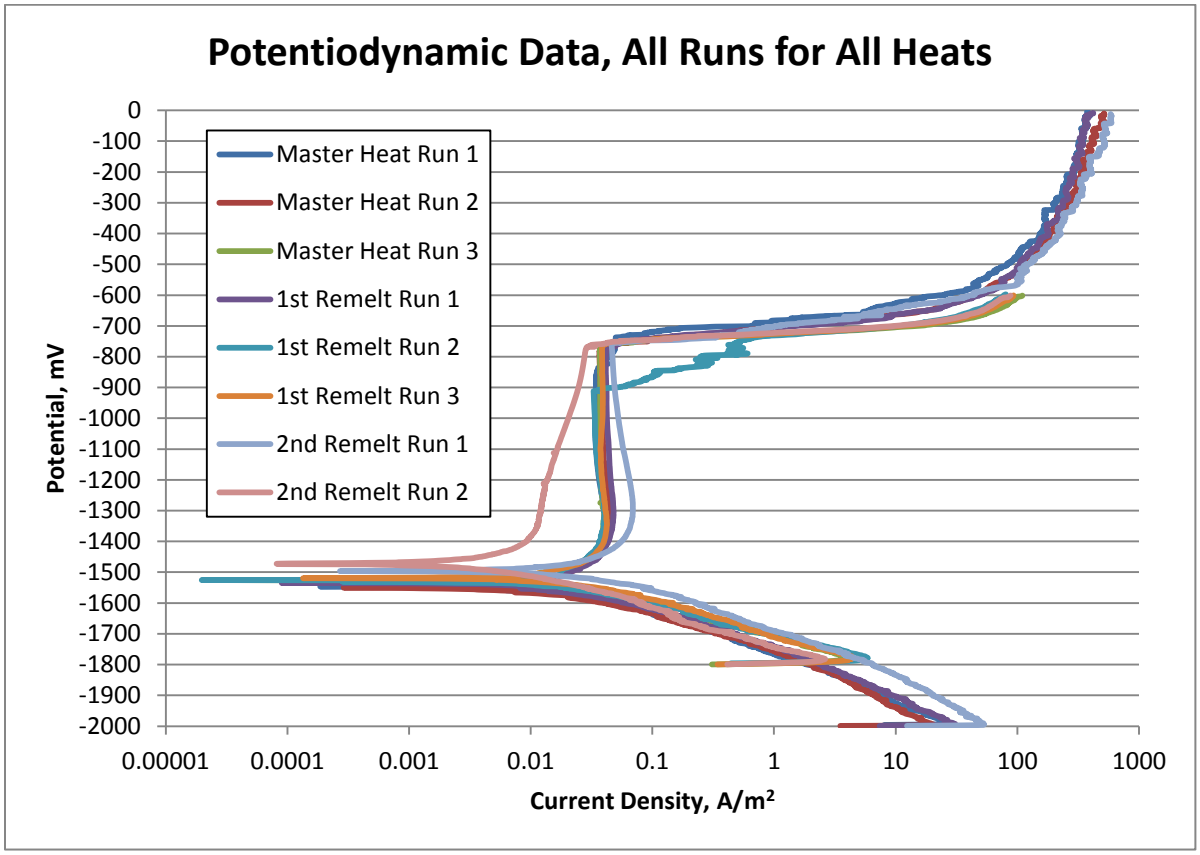

Figure 56: Data from all potentiodynamic runs

Appendix C: Potentiostatic Data

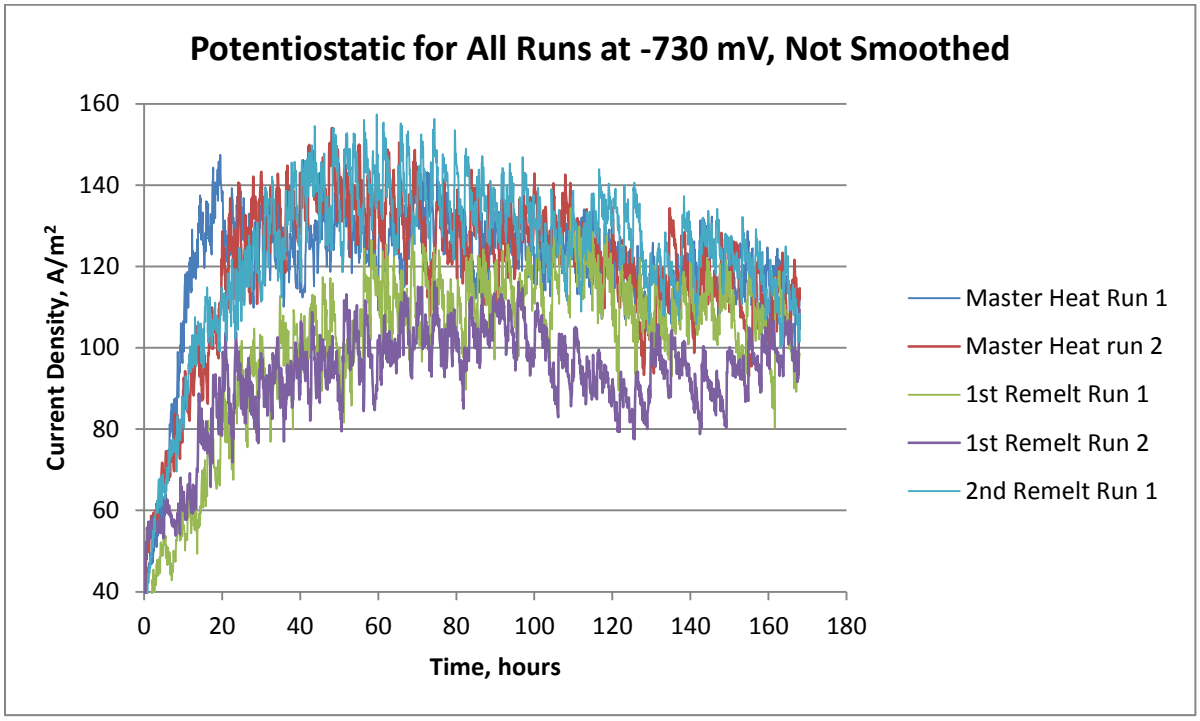

Figure 57: All potentiostatic runs, without smoothing

Appendix D: Galvanic Coupling Data

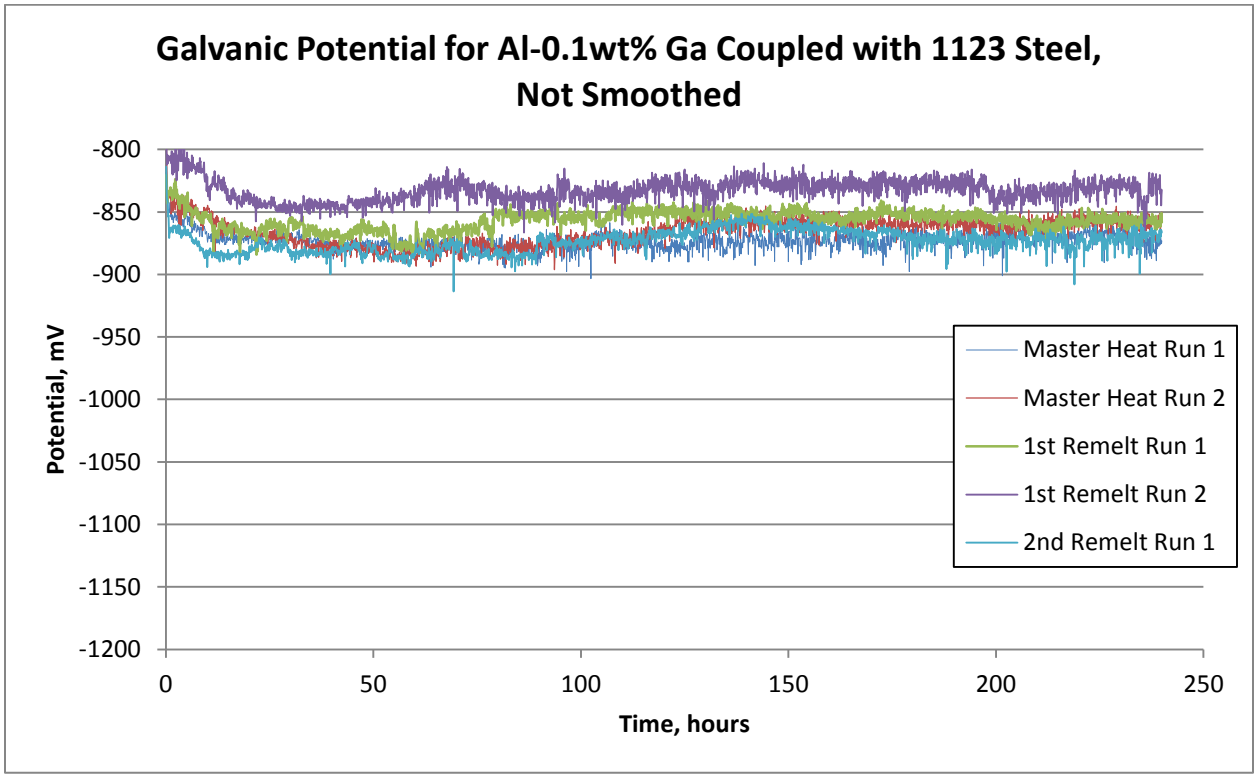

Figure 58: Galvanic Coupling potential data without smoothing

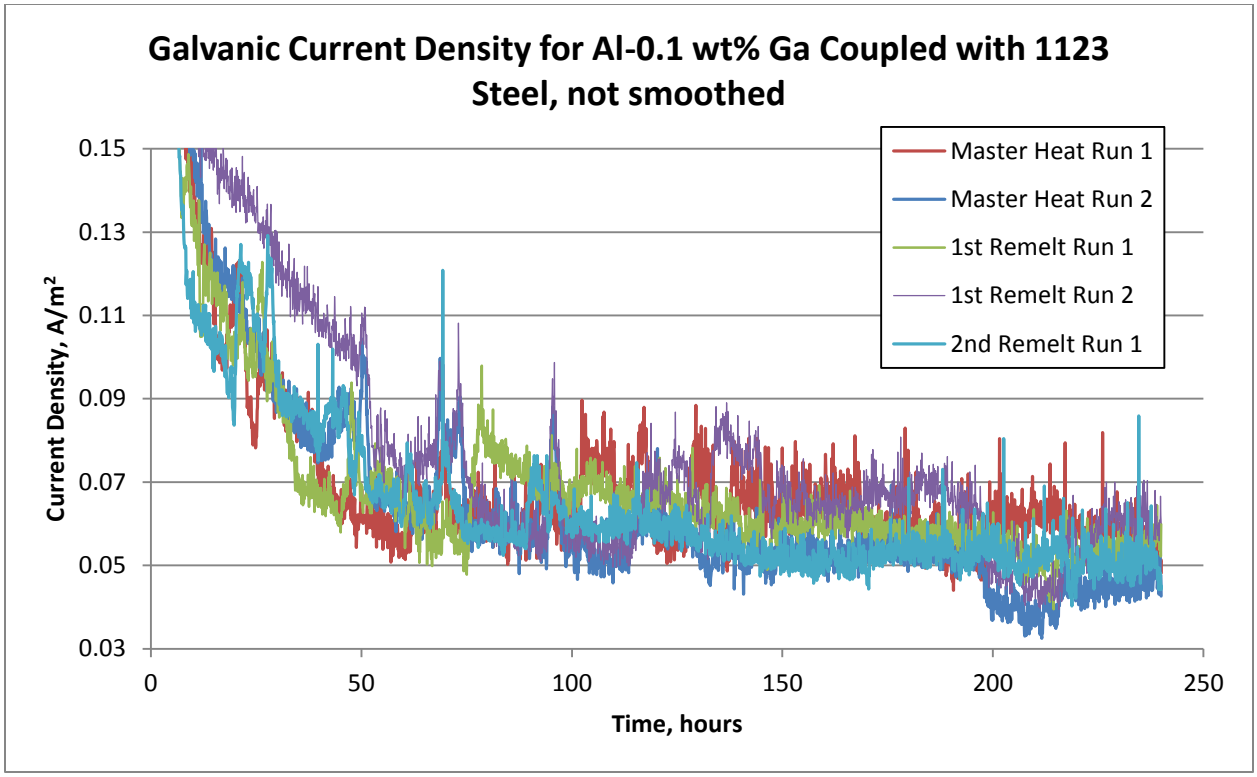

Figure 59: Galvanic Coupling current density data without smoothing

Appendix E: XPS Spectra

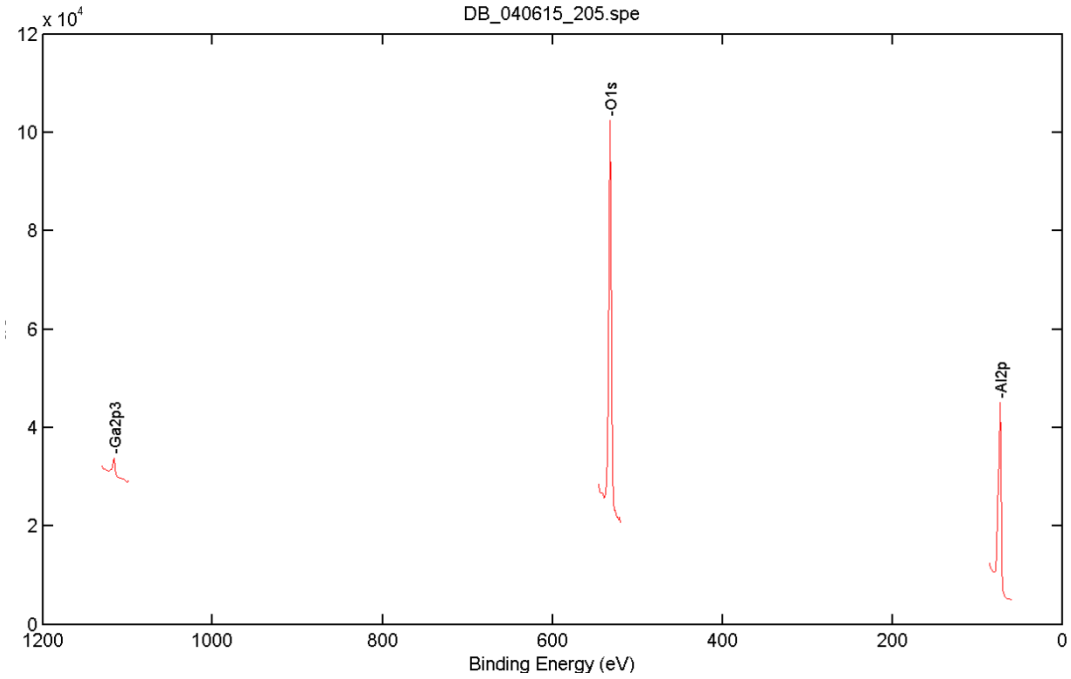

Figure 60: XPS data for uncorroded master heat after 1 min sputter at 3keV, with visible Ga peak

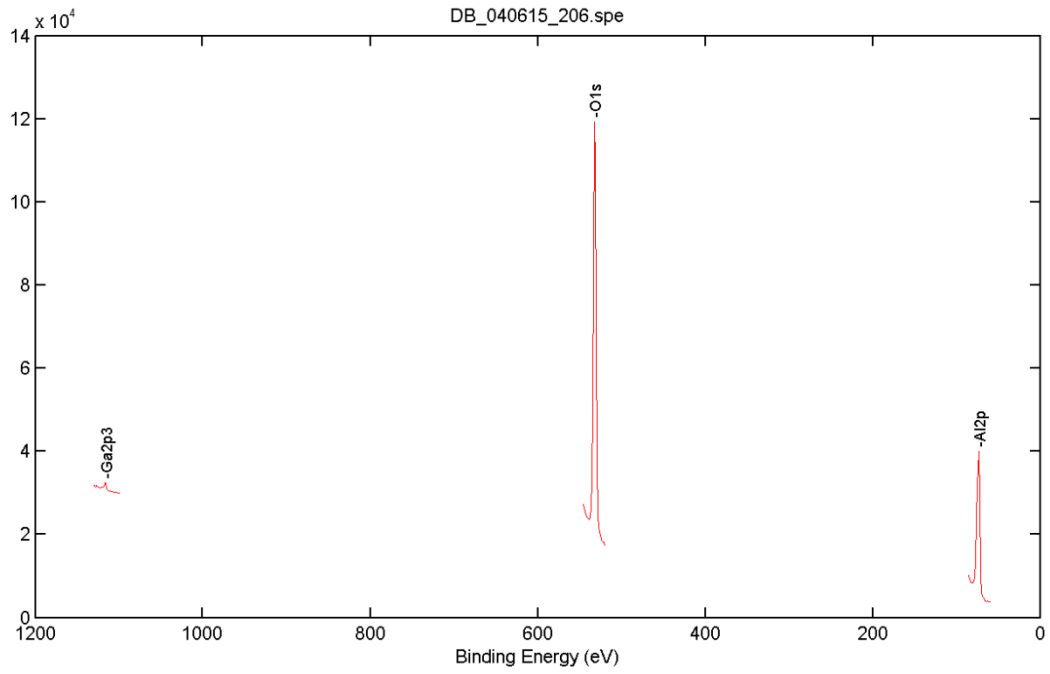

Figure 61: XPS data for uncorroded 1st remelt after 1 min sputter at 3keV, with visible Ga peak

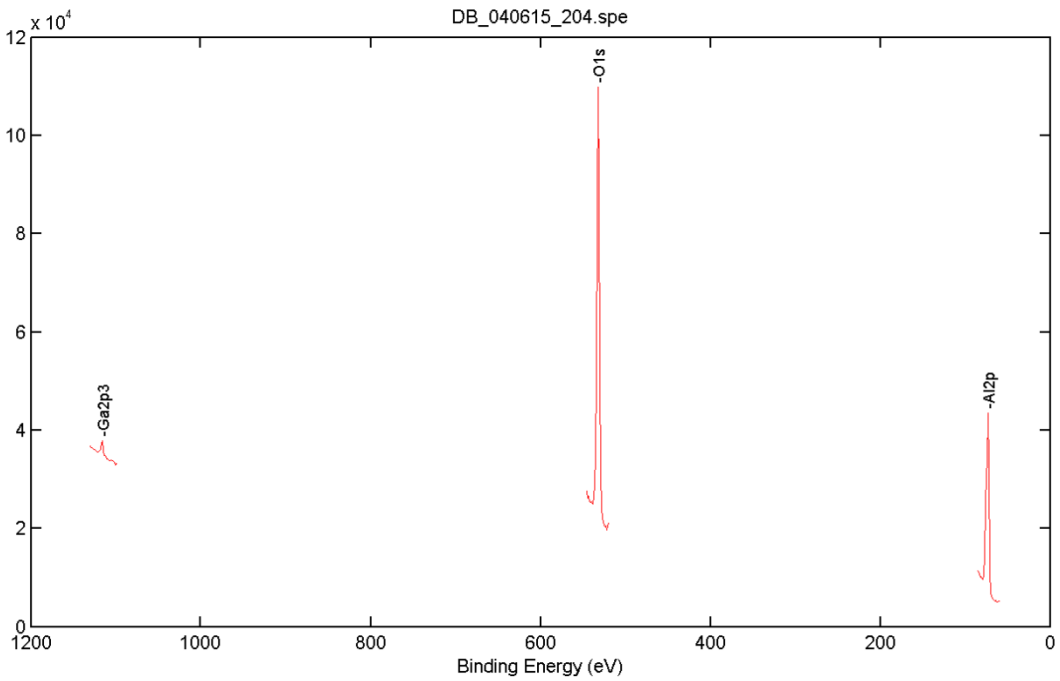

Figure 62: XPS data for uncorroded 2nd remelt after 1 min sputter at 3keV, with visible Ga peak